MPPT Reactive Control Algorithm for Heaving Wave Energy Converters with Power Setpoint Capabilities

Elamin, Abdin Y.; Wahyudie, Addy; Hashfi, Tuanku Badzlin; Shareef, Hussain; Errouissi, Rachid; Laghari, Mohammad Shakeel; Mubin, Marizan Binti; Mekhilef, Saad

DOI
10.1109/ACCESS.2024.3505422

Publication date
2024

Document Version
Final published version

Published in
IEEE Access

IEEE Access
Multidisciplinary ⋮ Rapid Review ⋮ Open Access Journal

Received 2 November 2024, accepted 19 November 2024, date of publication 25 November 2024,
date of current version 4 December 2024.

Digital Object Identifier 10.1109/ACCESS.2024.3505422

RESEARCH ARTICLE

MPPT Reactive Control Algorithm for Heaving Wave Energy Converters With Power Setpoint Capabilities

ABDIN Y. ELAMIN[1], (Graduate Student Member, IEEE), ADDY WAHYUDIE[1,2], (Member, IEEE), TUANKU BADZLIN HASHFI[3], HUSSAIN SHAREEF[1], (Member, IEEE), RACHID ERROUISSI[1], (Senior Member, IEEE), MOHAMMAD SHAKEEL LAGHARI[1], MARIZAN BINTI MUBIN[4], AND SAAD MEKHILEF[5], (Fellow, IEEE)

[1]Department of Electrical and Communication Engineering, United Arab Emirates University (UAE-U), Al Ain, United Arab Emirates
[2]National Water and Energy Center, United Arab Emirates University (UAE-U), Al Ain, United Arab Emirates
[3]Department of Electrical Sustainable Energy, Delft University of Technology, 2628 CD Delft, Netherlands
[4]Department of Electrical Engineering, Universiti Malaya, Kuala Lumpur 50603, Malaysia
[5]School of Science, Computing and Engineering Technologies, Swinburne University of Technology, Melbourne, VIC 3122, Australia

Corresponding author: Addy Wahyudie (addy.w@uaeu.ac.ae)

This work was supported in part by the United Arab Emirates University (UAE-U) Ph.D. Fund under Grant 31N387, and in part by the Asian University Alliance (AUA)-UAE-U Fund under Grant 12R181.

ABSTRACT Reactive control is a popular method for maximizing wave energy absorption in wave energy converters (WECs). This technique involves adjusting the damping and stiffness coefficients of the WEC to align its natural frequency with the frequency of incoming waves. Unfortunately, wave variability and complex hydrodynamics have posed challenges in accurately determining these coefficients. This paper proposes a model-independent approach for reactive control based on a variable step size maximum power point tracking (MPPT) algorithm. The MPPT algorithm tunes the WEC's damping and stiffness coefficients toward maximum generated power. Furthermore, a power curtailment control (PCC) strategy is integrated, based on a proportional-integral (PI) controller that modifies the MPPT control force to follow power generation references below its maximum generation capacity. This capability is essential for grid integration, where power generation must match demand. Finally, a hardware-in-the-loop experimental setup was constructed to evaluate the proposed control strategies under monochromatic and polychromatic wave conditions. An analysis comparing MPPT and damping control under various polychromatic wave conditions revealed that MPPT achieves substantially higher electrical power, outperforming damping control by 55.4% to 70.6%. The experimental results demonstrated the efficacy of the PCC strategy in reducing the WEC power output to track specific power setpoints.

INDEX TERMS Complex conjugate control, hardware-in-the-loop, maximum power point tracking, permanent magnet linear generator, perturb and observe algorithm, power curtailment control, wave energy converter.

I. INTRODUCTION

Recent concerns over increasing global power demands, carbon emissions, and climate change have encouraged the use of renewable energy sources (RESs) to fulfil global electric needs. In 2019, RES accounted for 27.3% of the globally produced electricity, with 90% being from wind, solar, and hydropower sources [1]. Wave energy is gradually attracting significant attention as an RES option because of its estimated annual potential of 151,300 TWh, high availability at coastlines sites, and high energy density [2], [3].

The associate editor coordinating the review of this manuscript and approving it for publication was Santu Giri.

A device that can transform wave energy into electricity is called a wave energy converter (WEC). A popular type of WEC is a heaving WEC which undergoes heaving motion during wave-body interaction to generate power [4]. Other types of WECs have been proposed and categorized based on either their power-capturing principles, such as oscillating water columns [5] or overtopping devices [6]; location of deployment, namely nearshore or offshore; or power take-off principles, such as electrical drives and hydraulic or mechanical systems [7]. However, WECs are still immature, and there is a lack of consensus on which type is superior in terms of performance, technical feasibility, and commercial viability [8].

Two main challenges must be addressed for WECs to reach a high level of maturity for adoption. The first focuses on maximizing wave energy absorption, whereas the second involves enhancing its role in the generation adequacy within the interconnected power system [9], [10]. Generation adequacy refers to the ability of the power system to balance between varying power generation and varying power demands [11]. These problems are complicated because wave energy has unwanted characteristics, such as (1) intermittency; (2) unpredictability; (3) location restraint; (4) low or no physical inertia; (5) non-dispatchability [9].

Control strategies can maximize wave energy absorption by utilizing a control force that will alter the WEC's velocity to have the same phase as the incident wave excitation forces [12]. Damping control modifies the power take-off (PTO) damping coefficient to maintain the phase difference between the buoy velocity and the excitation force close to zero [13]. Despite damping control being the default choice for evaluating WEC prototypes, it absorbs the least amount of wave energy compared to reactive control strategies [14], [15]. Reactive control can achieve better energy absorption but requires tuning two coefficients, namely the PTO damping and stiffness [16], [17]. This method necessitates bidirectional power flow, enabling the WEC to function alternately as a generator and motor within a single wave cycle. While this enhances absorption efficiency, it is prone to dissipative energy losses that may reduce the overall power output [18]. Unfortunately, both approaches struggle to precisely ascertain the optimal damping and stiffness coefficients due to their reliance on wave frequency, which is difficult to obtain in actual varying wave conditions. A feasible solution involves tuning the coefficients to accommodate the peak wave frequency [16]. Few research studies have explored model-free control approaches that are independent of wave frequency acquisition to obtain these coefficients. A maximum power point tracking algorithm (MPPT) for damping control was found in [19] and [20], where the MPPT was used to determine the duty cycle of the boost converters for maximum energy absorption. An evaluative study was conducted by [21] to investigate the factors impacting MPPT-based damping control in wave energy. In [22], a hill-climbing method is used to realize an MPPT for reactive control. The MPPT adjusted the damping and stiffness coefficients in the direction of maximum energy absorption, however, its performance in polychromatic sea waves was not investigated. Reinforcement learning was used in [18] to calculate these coefficients using a Q learning algorithm, whereas an artificial neural network and a fuzzy logic control were used in [23] and [24]. Alternative control strategies to enhance wave energy absorption, bypassing the computation of stiffness and damping coefficients, include approaches such as model predictive control, dynamic programming, proportional derivative version of complex conjugate control, and linear quadratic control [25], [26]. However, they are model-based control approaches, which make them susceptible to model inaccuracies and may require current and future wave excitation force knowledge. Extended Kalman filters [27], [28] and artificial neural networks [29] were some algorithms proposed to predict and estimate the excitation force. However, both predictive algorithms required a high computational power. A practical approach was proposed in [30] and [31] where pre-tuned resonance circuits were installed to improve power absorption. The resonance circuits were only tuned for a single frequency of wave and could lead to a large size of components in the circuits.

Wave energy is a fluctuating power that depends on sea state conditions rather than a consumer power demand portfolio. This power imbalance between generation and demand degrades the power system's generation adequacy, especially in penetration levels above 20%, which can lead to serious problems such as harmonics, frequency deviation, overloads, loss of synchronism, and voltage collapse [32], [33], [34]. An experimental study at Ireland's national wave test site assessed the impact of rapid wave power fluctuations on grid stability [35]. High penetration levels of RESs, such as wind and solar, have necessitated transmission system operators and distribution system operators to impose power generation setpoints based on grid power capacity and consumer demands [36]. While concerns about generation adequacy remain relatively subdued in wave energy systems due to their current low penetration levels, similar power setpoints are expected to be imposed following their further contribution to the grid.

A pragmatic solution for WECs to follow a specific power reference can be achieved by using energy storage systems (ESS). ESS can increase the utilization of this intermittent source by absorbing excess generated power and delivering the stored power during generation shortfalls. In addition, it can used to improve power quality by smoothing power fluctuations [37] or provide assisting services to the power system, such as frequency and voltage regulation [38]. Examples of ESSs used in WEC applications include hydraulic energy storage [39], supercapacitors [40], and hybrid energy storage systems [37]. However, complete dependence on ESS can cause two significant weaknesses: (1) the size of the ESS will increase when larger scale WECs are deployed, which consequently increases cost; (2) the ESS lifespan will degrade

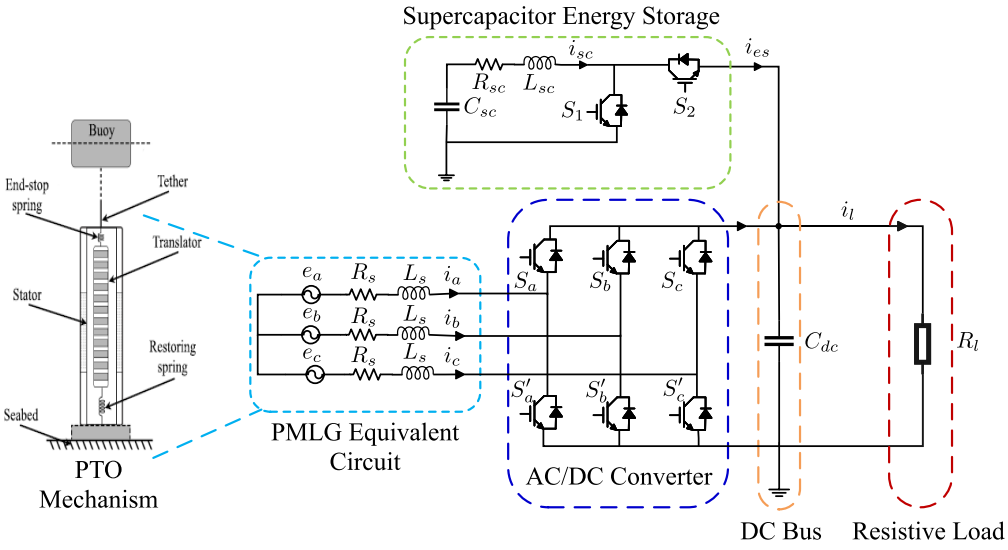

FIGURE 1. Schematic of the heaving WEC system.

when repeatedly charged and discharged [41]. Therefore, WECs that provide power curtailment control (PCC) without complete ESS dependency will be highly beneficial for grid integration. PCC allows WECs to govern the amount of power generated and follow power setpoint commands. This requires the WEC to operate at a range below its maximum power generation so that there is a reserve power available to follow the varying power setpoint commands. Substantial amounts of PCC strategies were implemented for wind power [42] and solar power [43]. In terms of WECs, the work of [41] proposed an active power setpoint tracking strategy based on a model predictive control algorithm for a six-degree-of-freedom WEC. Although the algorithm proved to mitigate the dependence of ESS under various sea conditions, the work is in its preliminary stage and has not been optimized for real-time application. In conclusion, the limited documented studies of PCC for WECs are primarily due to the ongoing developmental stage of these technologies for large-scale energy generation.

This paper proposes a hierarchical wave energy extraction control strategy for a heaving WEC. The control strategy allows the heaving WEC to shift between two operation modes: maximum power generation and following of the power setpoint. Maximum power generation is achieved by a reactive control strategy based on a variable step size MPPT algorithm for tuning the damping and stiffness coefficients that determine the control force. Furthermore, a PCC is introduced based on a proportional-integral (PI) controller that modulates the control force calculated from the MPPT algorithm, thereby reducing the WEC generated power to track a power reference. In addition, the WEC consists of a supplementary ESS to provide reactive control support and regulate the DC bus voltage. A super capacitor bank is selected as the energy storage element because of its longevity, high power density, robust operating limits, and fast charge and discharge rates. A cascaded two PI control loop structure is used to control the ESS. Finally, a hardware-in-the-loop (HIL) setup is designed to validate the proposed control algorithms experimentally.

The contribution of this study is twofold. The first is to design a simple and computationally inexpensive WEC reactive control strategy for maximum power generation. The second involves enabling the WEC to act as a controllable power source that follows power commands by adopting a simple PCC strategy that is less dependent on ESS and feasible for real-time applications.

The remainder of this paper is organized as follows: Section II describes the modeling of the WEC and the super capacitor ESS. Section III discusses the control framework adopted for power maximization, power setpoint following, and ESS control. Section IV presents the experimental results and discussion. Finally, conclusions are presented in Section V.

II. MATHEMATICAL MODEL OF THE WEC SYSTEM

This section provides a detailed wave-to-wire description and model of the heaving WEC under investigation. As shown in Fig. 1, the WEC includes a floating cylindrical buoy that moves vertically in the presence of incident waves. The heaving motion of the buoy directly moves the PMLG's translator causing electrical power to be generated at the PMLG output terminals. The PMLG with the AC/DC power converter makes up the PTO mechanism of the WEC. The PTO is in charge of converting the captured wave mechanical power into electrical power and acts as an actuator for altering the buoy motion in control applications. In addition, an auxiliary ESS containing a supercapacitor and a bi-directional DC/DC converter is connected to the PTO via

a DC bus. A resistive load on the DC bus's right side is used to dissipate the generated power.

The polychromatic nature of the sea waves and their associated energy characteristics are formulated and modeled through wave spectrum analysis. The mathematical model of the heaving WEC is divided into three sub-models: the hydrodynamic model, the electrical model, and the supercapacitor energy storage model. The hydrodynamic model describes the WEC's heaving motion caused by sea waves and its associated hydrodynamic forces. By contrast, the electrical model represents the PMLG's mathematical description and defines the PTO-controlled electromagnetic force. Finally, the supercapacitor energy storage model includes the mathematical description of the supercapacitor, bidirectional DC/DC converter, and the power exchange relations at the DC bus.

A. WAVE SPECTRUM

Sea waves are mainly created by wind blowing over the sea surface [3]. Monochromatic sea waves, characterized by a single frequency and amplitude, serve as simplified and predictable representations of sea waves. However, real sea waves are typically polychromatic and irregular, encompassing diverse frequencies and amplitudes that more accurately capture the complexity and variability of real sea conditions. While monochromatic waves simplify the analysis, polychromatic waves represent the real-world challenges in wave dynamics and energy conversion studies. Superposition theory can be applied to represent polychromatic wave profiles as a summation of several sinusoidal waves of different phases, frequencies, and amplitudes [3], as follows

$$\xi(t) = \sum_{i=1}^{N_w} \alpha_i \cos(\omega_i t + \theta_i) \tag{1}$$

where ξ, ω_i, α_i, and θ are the wave surface elevation, angular frequency, amplitude, and phase of the ith harmonic wave, respectively. The variable N_w denotes the number of sinusoidal waves.

Wave spectrums that show the variation of wave energy, with respect to frequency, can be adopted to represent polychromatic wave profiles. Additionally, they convey wave information such as height, frequency, and energy transport. Several wave spectrums were proposed, such as the Pierson-Moscowitz (PM) [44] and Joint North Sea Wave Observation Project (JONSWAP) [45]. PM spectrum is used in this work because it is the most suitable to characterize fully developed sea states. By specifying significant wave height and peak wave period, a modified PM spectrum is described by the following:

$$S(\omega) = \frac{5\pi^4 H_s^2}{T_p^4 \omega^5} \exp\left(-\frac{20\pi^4}{T_p^4 \omega^4}\right) \tag{2}$$

where ω, T_p and H_s are the wave angular frequency in radians per second, peak wave period and significant wave height, respectively. The nth spectral moment is given by the following:

$$m_n = \int_0^\infty \omega^n S(\omega) d\omega \tag{3}$$

and the wave energy period is calculated as follows:

$$T_e = \frac{m_{-1}}{m_0}. \tag{4}$$

The wave energy transport J defined as the power density per unit width of wave front, is given as follows:

$$J = \frac{\rho g^2 T_e H_s^2}{64\pi} \tag{5}$$

where ρ is the sea water density and g is the acceleration due to gravity [12]. Equation (5) is used for polychromatic waves, but can be modified to address monochromatic waves as follows:

$$J = \frac{\rho g^2 T H^2}{32\pi}. \tag{6}$$

with T is the wave period and H is the wave height, which is equal to twice of amplitude of the wave. In addition, the average available wave power $\bar{P}_w$ is bounded by the wave energy transport as follows:

$$\bar{P}_w < J \cdot D \tag{7}$$

where D represents the buoy diameter.

B. HYDRODYNAMIC MODEL

Although the floating cylindrical buoy is free to move in all directions on the sea surface, only the heaving motion is considered because of the insignificant influences of other motions [46]. The forces acting on the buoy in the heave direction can be expressed, in terms of Newton's second law of motion, as follows:

$$M\ddot{z}(t) = f_{ex}(t) - f_r(t) - f_b(t) - f_{rs}(t) + f_u(t) \tag{8}$$

where M denotes the total mass of moving parts (buoy, tether and translator) and $\ddot{z}(t)$ is the heave acceleration. Whereas $f_{ex}(t), f_r(t), f_b(t), f_{rs}(t)$, and $f_u(t)$ represent the wave excitation force, radiation force, hydrostatic buoyancy force, restoring spring force and PTO controlled electromagnetic force, respectively. The excitation force $f_{ex}(t)$ is modeled in the time domain as follows:

$$f_{ex}(t) = k_{ex}(t) * \xi(t) = \int_0^t k_{ex}(\tau)\xi(t-\tau)d\tau \tag{9}$$

here, $k_{ex}(t)$ is the excitation kernel function and $\xi(t)$ is the wave elevation. Equation (7) can be represented in the frequency domain by applying Fourier transformation, as follows:

$$F_{ex}(i\omega) = K_{ex}(i\omega)\Xi(i\omega) \tag{10}$$

$\Xi(i\omega)$ denotes the Fourier transformation of wave elevation, whereas $K_{ex}(i\omega)$ is for the excitation kernel function, whereas $\Xi(i\omega)$ denotes the wave elevation. The WAMIT software is

used to approximate the $K_{ex}(i\omega)$ with a finite order transfer function having the following form:

$$K_{ex}(s) = \frac{b_m s^m + b_{m-1}s^{m-1} + \ldots + b_0}{a_n s^n + a_{n-1}s^{n-1} + \ldots + a_0} \tag{11}$$

where m and n are the orders of the numerator and denominator, respectively. Variable s is the Laplace complex variable, whereas b_m, b_{m-1}, b_0, a_n, a_{n-1} and a_0 are the transfer function coefficients. Likewise, the radiation force can be written in the time domain as follows:

$$f_r(t) = -m_\infty \ddot{z}(t) - \int_0^t k_r(\tau)\dot{z}(t-\tau)d\tau \tag{12}$$

where the added mass, radiation kernel function and heave velocity are denoted by m_∞, $k_r(\tau)$ and $\dot{z}(t)$, respectively. The radiation kernel function can be related to the radiation damping $B_r(\omega)$ and the radiation added mass $M_r(\omega)$ in the frequency domain as follows:

$$K_r(\omega) = B_r(\omega) + \omega[M_r(\omega) - m_\infty]. \tag{13}$$

WAMIT is used to approximate the radiation damping $B_r(\omega)$ and the radiation added mass $M_r(\omega)$. Taking the Fourier transform of (11) and using (12), the frequency domain representation of the radiation force $F_r(\omega)$ is obtained as follows:

$$F_r(\omega) = -[B_r(\omega) + \omega M_r(\omega)]V(\omega) \tag{14}$$

where $V(\omega)$ denotes the heave velocity in the frequency domain. The hydrostatic buoyancy and restoring spring forces are modeled linearly as stiffness forces using the following:

$$f_b(t) = C_b z(t) = \rho g A_w \tag{15}$$

$$f_{rs}(t) = C_{rs} z(t) \tag{16}$$

where C_b, C_{rs}, $z(t)$ and A_w are the buoyancy stiffness coefficient, restoring spring stiffness coefficient, heave displacement and buoy submerged surface area. Taking the Fourier transform of (8), the forces to heave velocity model in the frequency domain is obtained as follows:

$$\frac{V(\omega)}{F_{ex}(\omega) + F_u(\omega)} = \frac{1}{Z_i(\omega)} \tag{17}$$

where $F_u(\omega)$ and $F_{ex}(\omega)$ are the Fourier transform of the PTO control force and excitation force, respectively. Whereas $Z_i(\omega)$ is the WEC intrinsic impedance, given by the following:

$$Z_i(\omega) = B_r(\omega) + \omega\left[M + M_r(\omega) - \frac{c_b + c_{rs}}{\omega}\right]. \tag{18}$$

C. ELECTRICAL MODEL

The PMLG is similar to the rotary permanent magnet generator, except the permanent magnets located in the translator reciprocate in a linear motion. Its increased reliability and efficiency, stemming from a more robust driving force, makes it better suited for wave energy conversion than other linear generator types [47]. Various topologies of PMLGs have been explored, including the planar or flat-type, which is favored in high-power applications. Conversely, the tubular-type topology is deemed appropriate for low-power applications because it delivers high power or force density. The studies in [48] and [49] offer a comprehensive methodology for designing tubular PMLGs for wave energy production. The work of [48] also includes a comparative analysis between two distinct types: an inner permanent magnet slotted tubular linear generator and an outer permanent magnet slot less tubular linear generator. However, despite the variety in PMLG topologies, they all operate on a similar principle, relying on a buoy that moves freely on the ocean surface in response to wave-induced motions. The translator mimics this heaving motion, influenced by the coupling effect of the tether.

The angular position of the system $\theta(t)$ is then defined as a function of the heave displacement $z(t)$ as follows

$$\theta(t) = \frac{\pi}{\tau_p} z(t). \tag{19}$$

The heave movement causes a net flux $\phi(t)$ in the PMLG coils given by the following:

$$\phi(t) = \phi_m \sin\left(\frac{\pi}{\tau_p} z(t)\right) \tag{20}$$

where ϕ_{pm} and τ_p are the permanent magnet flux linkage and the PMLG's pole pitch, respectively. Voltage is induced in the stator coils due to the change of that magnetic flux [50]. For a three phase PMLG, induced electromotive force voltages (EMF) in the abc frame, $e(t) = [e_a(t) \quad e_b(t) \quad e_c(t)]^T$, is calculated by the following:

$$e_a(t) = -N_p \frac{\pi \phi_{pm}}{\tau_p} \dot{z}(t) \sin\left(\frac{\pi}{\tau_p} z(t)\right) \tag{21}$$

$$e_b(t) = -N_p \frac{\pi \phi_{pm}}{\tau_p} \dot{z}(t) \sin\left(\frac{\pi}{\tau_p} z(t) - \frac{2\pi}{3}\right) \tag{22}$$

$$e_c(t) = -N_p \frac{\pi \phi_{pm}}{\tau_p} \dot{z}(t) \sin\left(\frac{\pi}{\tau_p} z(t) + \frac{2\pi}{3}\right) \tag{23}$$

where N_p represents the number of turns per phase. The dynamic model of the PMLG in the abc frame is given as follows:

$$e(t) = R_s \mathbf{i_s}(t) + j\omega_e(t) L_s \mathbf{i_s}(t) + \mathbf{v_s}(t) \tag{24}$$

where $\mathbf{i_s}(t) = [i_{sa}(t) \; i_{sb}(t) \; i_{sc}(t)]^T$, R_s, L_s, and $\mathbf{v_s}(t) = [(v_{sa}(t) \; v_{sb}(t) \; v_{sc}(t)]^T$ are the three phase stator currents, stator resistance, stator inductance and the three phase voltage terminals. Whereas $\omega_e(t)$ is the angular frequency calculated by differentiating (19)

$$\omega_e(t) = \frac{\pi}{\tau_p} \dot{z}(t). \tag{25}$$

Assuming the PMLG is surface mount and symmetric, the Park-Clarke transformation can be used to express its dynamic model in the synchronous reference (d-q)

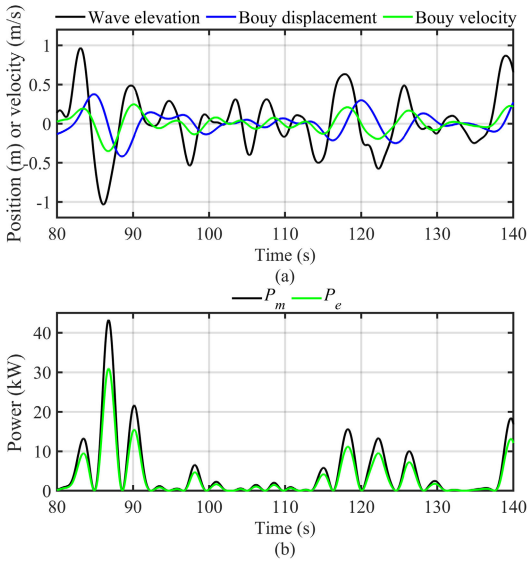

FIGURE 2. WEC dynamic without a maximum energy extraction: (a) wave's elevation, buoy's displacement, and buoy's velocity, (b) power plots.

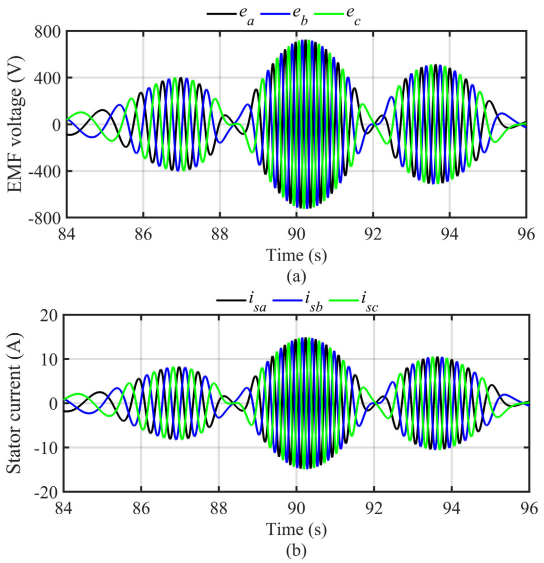

FIGURE 3. PMLG electrical characteristics without a maximum energy extraction controller: (a) EMF voltages, (b) stator currents.

frame [51], as follows:

$$\frac{di_{sd}(t)}{dt} = \frac{-R_s i_{sd}(t)}{L_s} + \omega_e(t) i_{sq}(t) - \frac{v_{sd}(t)}{L_s} \tag{26}$$

$$\frac{di_{sq}(t)}{dt} = \frac{-R_s i_{sq}(t)}{L_s} - \omega_e(t) i_{sd}(t) - \frac{\omega_e(t)}{L_s}\phi_{pm} - \frac{v_{sq}(t)}{L_s} \tag{27}$$

where $i_{sd}(t)$ and $i_{sq}(t)$ are the direct and quadrature components of the stator current, whereas $v_{sd}(t)$ and $v_{sq}(t)$ are the d-q components of terminal voltages.

The PTO controlled electromagnetic force depends on the quadrature stator current, as shown below:

$$f_u(t) = \frac{3\pi\phi_{pm}}{2\tau_p} i_{sq}(t). \tag{28}$$

The instantaneous absorbed mechanical power $P_m(t)$, generated electrical power $P_e(t)$ and instantaneous copper power loss due to the PMLG's stator coils $P_{loss}(t)$ are calculated as follows:

$$P_m(t) = f_u(t)\dot{z}(t) = \frac{3\pi\phi_{pm}}{2\tau_p} i_{sq}(t)\dot{z}(t) \tag{29}$$

$$P_e(t) = \frac{3}{2}\left(v_{sd}(t) i_{sd}(t) + v_{sq}(t) i_{sq}(t)\right) \tag{30}$$

$$P_{loss}(t) = \frac{3}{2} R_s \left(i_{sd}^2(t) + i_{sq}^2(t)\right). \tag{31}$$

Figure 2 illustrates the behavior of a heaving WEC, with part (a) showing its kinematics and part (b) depicting its power output. These figures assume the WEC operates without a wave energy extraction controller under the influence of a polychromatic wave of significant height $H_s = 2$ m and an energy period of $T_e = 10$ s. Figure 2a details the buoy's dynamics relative to wave elevation. An increase in wave elevation results in an upward movement of the buoy, indicated by a rise in its position and an upward velocity. Conversely, a decrease in wave elevation causes the buoy to descend, marked by a decrease in its position and a downward velocity. Figure 2b shows the phase alignment of generated power with absorbed power, albeit at a reduced magnitude due to copper losses in the PMLG.At 86.8 s, the absorbed power reaches a peak of 43.1 kW, corresponding to the buoy's maximum downward velocity of 0.35 m/s, while the maximum generated power approaches 30.1 kW. Figure 3 depicts the three-phase EMF voltages and stator currents of the PMLG. At peak power generation, the EMF voltages recorded a peak value of 722.9 V, while the stator currents reached a maximum of 14.8 A. An irregular sine waveform with variable magnitude and frequency is evident in both voltages and currents. This behavior arises from the reciprocating motion of the translator within the PMLG. Variations in translator velocity during oscillation cause corresponding changes in the amplitude and frequency of the voltages and currents [49]. Furthermore, the inherent fluctuations in wave energy, which drives the PMLG, further amplify the alternating characteristics of these electrical quantities.

D. SUPERCAPACITOR ENERGY STORAGE MODEL

The bidirectional power flow nature of reactive control requires excessive negative power to be delivered to the PTO at some instance of time, particularly during startups. This negative power will be provided by the supercapacitor energy storage system (ESS). The DC bus represents the connection point between the PTO mechanism, the ESS, and the load. As a result, it is subjected to voltage variations caused by power discrepancies expressed by the following

power exchange equation:

$$C_{dc}v_{ds}(t)\frac{dv_{dc}(t)}{dt} = P_e(t) + P_{sc}(t) - p_l(t) \tag{32}$$

as

$$P_{sc}(t) = i_{es}(t) \cdot v_{dc}(t) \tag{33}$$

$$P_l(t) = i_l^2(t) \cdot R_l \tag{34}$$

where C_{dc}, $P_{sc}(t)$, $P_l(t)$, $i_{es}(t)$, and R_l represent the DC bus capacitance, energy storage delivered power, consumed load power, supercapacitor output current, load current and load resistance, respectively.

Supercapacitors are electrochemical energy storage elements characterized by their high capacitance levels and low voltage limits compared to conventional capacitors. The following describes the relationship between their stored energy and instantaneous voltage:

$$E_{sc}(t) = \frac{1}{2}C_{sc}v_{sc}(t) \tag{35}$$

$$v_{sc}(t) = v_0 \exp\left(-\frac{t}{R_{esc}C_{sc}}\right) \tag{36}$$

where $E_{sc}(t)$, C_{sc}, R_{esc}, $v_{sc}(t)$, and v_0 represent total energy stored, supercapacitor capacitance, supercapacitor equivalent series resistance, instantaneous supercapacitor voltage and initial supercapacitor voltage. Supercapacitors can be connected in series and/or parallel to form a bank that can achieve desired energy storage, voltage and capacitance requirements. In addition, the supercapacitor energy storage model includes a high frequency inductor L_{sc} and a bidirectional DC/DC converter that contains two IGBT switches S_1 and S_2. The supercapacitor energy storage operates in two modes determined by the DC bus voltage, namely charge and discharge modes.

The discharge mode is activated when the DC bus voltage falls below a specific voltage. During this mode, S_1 is on, S_2 is off, and the supercapacitor provides power to the DC bus ($i_{es} > 0$). Meanwhile, a rise in the DC bus voltage above a specific setpoint triggers the charge mode. In the charge mode, S_1 is off, and S_2 is on; the supercapacitor absorbs the excessive power for charging ($i_{es} < 0$). The energy storage model during discharge is given as follows:

$$\frac{di_{sc}(t)}{dt} = \frac{v_{sc}(t)}{L_{sc}} - \frac{R_{sc}}{L_{sc}}i_{sc}(t) - \frac{(1-u_1)v_{dc}(t)}{L_{sc}} \tag{37}$$

while during charging the model becomes

$$\frac{di_{sc}(t)}{dt} = \frac{v_{sc}(t)}{L_{sc}} - \frac{R_{sc}}{L_{sc}}i_{sc}(t) - \frac{(u_2)v_{dc}(t)}{L_{sc}} \tag{38}$$

here, i_{sc} is the supercapacitor input current and R_{sc} is the intrinsic resistance of the inductor. Whereas u_1 and u_2 are the control signals for S_1 and S_2, respectively. It is possible to combine (37) and (38) in a generic model by introducing the control signal u_{12} [52].

$$u_{12} = [S(1-u_1) + (1-s)u_2] \tag{39}$$

where

$$S = \begin{cases} 1, & \text{in discharging mode} \\ 0, & \text{in charging mode.} \end{cases} \tag{40}$$

Finally, the generic model is expressed as follows:

$$\frac{di_{sc}(t)}{dt} = \frac{v_{sc}(t)}{L_{sc}} - \frac{R_{sc}}{L_{sc}}i_{sc}(t) - \frac{(u_{12})v_{dc}(t)}{L_{sc}} \tag{41}$$

$$i_{es}(t) = u_{12}i_{sc}(t). \tag{42}$$

III. PROPOSED CONTROL METHOD

This section emphasizes the wave energy extraction control strategy for the heaving WEC. The control strategy adopts a hierarchical structure consisting of two control levels. The objective of the upper level is to calculate the PTO control force, whereas the lower control level implements the control force set by the the upper level. The upper control level uses the MPPT reactive control algorithm to compute the PTO control force f_u^{mppt} for maximum power generation. Although the MPPT algorithm is sufficient for maximum power generation, the algorithm does not provide power curtailment control (PPC). Therefore, a proportional-integral (PI)-based PCC is integrated into the higher control level. It is activated when the heaving WEC operates in the power-setpoint following mode. The PI PPC calculates the scale factor λ that curtails f_u^{mppt} and obtains the required control force f_u^{pc} to track the power reference. The lower level consists of two PI current controllers that realize the control force by regulating PMLG's stator currents.

Furthermore, an ESS controller is implemented to regulate the DC bus voltage by balancing the power exchange between the WEC and load. This objective provides reactive power support for the WEC while delivering constant power to the load. The ESS control structure consists of two cascaded PI controller loops that transmit the control signal to the sinusoidal pulse width modulation algorithm, which is then fed to the bi-directional DC/DC converter in the form of switching pulses.

A. PROPOSED MPPT REACTIVE CONTROL

To achieve maximum wave energy absorption, the controller must excite the WEC with a specific PTO control force so that the heave velocity is in resonance with the wave excitation force. Assuming the PTO control force in the frequency domain is defined as follows:

$$F_u(\omega) = Z_{pto}(\omega)V(\omega). \tag{43}$$

Substitution of (43) in (16) shows that this resonance occurs when the PTO impedance $Z_{pto}(\omega)$ equals the complex conjugate of the WEC intrinsic impedance $Z_i^*(\omega)$, or

$$Z_{pto}(\omega) = Z_i^*(\omega). \tag{44}$$

Equation (44) is known as complex conjugate control. However, this optimal control strategy is infeasible due to excessive heave movements due to the low WEC intrinsic damping $B_r(\omega)$. The extreme heave movements would

necessitate bigger and more expensive PMLG to handle the large strokes. Thus, practical suboptimal control alternatives, such as damping and reactive control, have been proposed. Damping control defines the PTO control force to be linearly proportional to the damping coefficient B_{pto} as shown in the following:

$$f_u(t) = -B_{pto}\dot{z}(t) \tag{45}$$

where

$$B_{pto} = |Z_i(\omega)|\,. \tag{46}$$

In reactive control, the PTO control force is expressed in terms of damping coefficient B_{pto} and stiffness coefficients K_{pto} as follows:

$$f_u(t) = -B_{pto}\dot{z}(t) - K_{pto}z(t). \tag{47}$$

Although reactive control is superior to damping control, its implementation faces some challenges. Optimal damping and stiffness coefficients can be easily computed in monochromatic waves, but it is difficult to compute such values for polychromatic waves because of their frequency fluctuation over time. Furthermore, although reactive control uses bidirectional power flow to maximize wave energy absorption, it does not always guarantee maximum power generation when excessive negative reactive power is required.

The proposed MPPT reactive control algorithm is implemented to search for the damping and stiffness coefficients that define the PTO control force for maximum WEC power generation. As seen in Fig. 2b, the varying instantaneous generated power makes it complicated for the MPPT algorithm to adjust to the optimal coefficients for maximum power generation consistently. Consequently, an alternative approach is adopted wherein the mean generated electrical power ($\bar{P}_e$) is chosen as the maximization target instead of the instantaneous value in (30) to avoid MPPT oscillations caused by rapid instantaneous power fluctuations. The $\bar{P}_e$ is calculated as follows:

$$\bar{P}_e = \frac{1}{N_s}\sum_{i=0}^{N_s} P_e(i) \tag{48}$$

where $P_e(i)$ denotes the instantaneous generated electrical power at sampling instant i and N_s is the number of samples.

For the MPPT algorithm to be effective, there should be a maximum mean generated power at optimal coefficient values B^*_{pto} and K^*_{pto}, as then the MPPT will update the variables such that $(B_{pto},\ K_{pto}) \rightarrow (B^*_{pto},\ K^*_{pto})$ [53]. Figure 4 displays the effect of varying damping and stiffness coefficients on the mean generated power when subjected to a monochromatic sea state with $H_s = 1$ m and $T_e = 9$ sec using parameters in Section IV-A. It is obvious that a maximum peak of 61.171 kW occurs at $B_{pto} = 147,368$ Ns/m and $K_{pto} = 112,500$ N/m. In terms of B_{pto}, it is noticed that values equal to zero do not generate power, and values below the optimal results in a steeper curve than higher values.

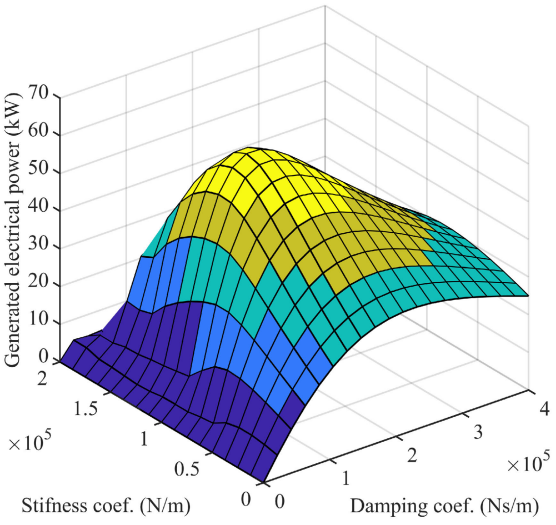

FIGURE 4. 3D curve of the WEC generated power subjected to damping and stiffness variations.

The reason being that B_{pto} is concerned with the ability of the WEC to absorb active power. Negative values of B_{pto} indicate that active power is released to the sea. Large values of B_{pto} increases the WEC resistance to move, which decreases the generated power. Regarding K_{pto}, zero values generate power but exceeding optimal values will result in a steeper decrease of generated power. Unlike B_{pto}, K_{pto} is concerned with the absorption of reactive power. Large values of K_{pto} increase the amount of required reactive power, which comes at the expense of the generated active power. Taking these effects of B_{pto} and K_{pto} into consideration, boundary limits must be defined, where $B_{pto} \in \left[0,\ B^{max}_{pto}\right]$ and $K_{pto} \in \left[0,\ K^{max}_{pto}\right]$.

In this MPPT, mean generated power is sampled every control period $T_{control}$ and coefficients are interchangeably updated toward the gradient direction that leads to maximum generated power. A flowchart of the proposed MPPT algorithm is shown in Fig. 5. If the iteration number of the control period k is odd, B_{pto} is updated based on the power and damping values obtained from prior periods, while K_{pto} remains unchanged, as shown below:

$$B_{pto}(k+1) = B_{pto}(k) + \mu(k)\cdot \text{sign}\left(\frac{\partial P_e}{\partial B_{pto}}\right) \tag{49}$$

$$K_{pto}(k+1) = K_{pto}(k) \tag{50}$$

when k is even, B_{pto} is unchanged, but K_{pto} is updated as follows:

$$B_{pto}(k+1) = B_{pto}(k) \tag{51}$$

$$K_{pto}(k+1) = K_{pto}(k) + \mu(k)\cdot \text{sign}\left(\frac{\partial P_e}{\partial K_{pto}}\right) \tag{52}$$

where $\mu(k)$ represents the step size at the update period iteration number k. The gradients can be approximated

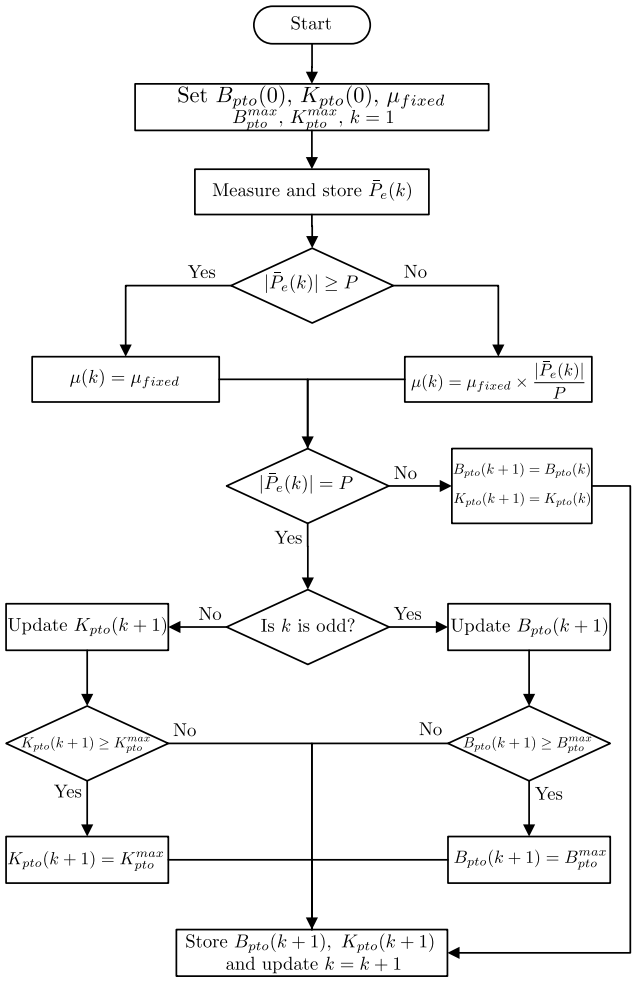

FIGURE 5. The flowchart for the proposed MPPT reactive control algorithm.

through first-order backward differencing as

$$\frac{\partial \bar{P}_e}{\partial B_{pto}} \approx \frac{\bar{P}_e(k) - \bar{P}_e(k-1)}{B_{pto}(k) - B_{pto}(k-1)} \tag{53}$$

$$\frac{\partial \bar{P}_e}{\partial K_{pto}} \approx \frac{\bar{P}_e(k) - \bar{P}_e(k-1)}{K_{pto}(k) - K_{pto}(k-1)} \tag{54}$$

Finally, the MPPT algorithm determines the PTO control force as follows

$$f_u^{mppt}(t) = -B_{pto}(k)\dot{z}(t) - K_{pto}(k)z(t). \tag{55}$$

To improve the MPPT performance, proper tuning must be taken in choosing the control rate and step size. The control rate $f_{control}$ is the reciprocal of the control period, and it defines the rate at which the MPPT responds to mean power output variations. The MPPT response can be accelerated using a faster control rate, allowing the maximum power point to be reached sooner. However, increasing the control rate, beyond a limit, can cause the MPPT to oscillate rapidly due to insufficient power measurements. To avoid this instability, the control period must be set at a constant greater than three times the wave period [22].

The step size μ governs how aggressively the MPPT algorithm reacts to variations in mean generated power. Selecting the step size is typically a trial-and-error process. A small step size results in a smaller dynamic response, increasing the transient power loss. By contrast, a large step size provides a faster response but introduces significant fluctuations near the maximum power region [54]. To address the step size selection, the MPPT adopts a variable step size defined by the following:

$$\mu(k) = \begin{cases} \mu_{fixed}, & \text{if } \left|\Delta \bar{P}_e(k) \geq P\right| \\ \mu_{fixed} \cdot \dfrac{\left|\Delta \bar{P}_e(k)\right|}{P}, & \text{if } \left|\Delta \bar{P}_e(k) < P\right| \end{cases} \tag{56}$$

where $\Delta \bar{P}_e(k)$ is the change in mean generated electrical power given by

$$\Delta \bar{P}_e(k) = \bar{P}_e(k) - \bar{P}_e(k-1). \tag{57}$$

A fixed step size μ_{fixed} is adopted when the distance is far from the maximum power point. When mean power approaches the maximum power point, $\Delta \bar{P}_e(k)$ decreases until its value is lower than the power difference threshold P and the step size decreases with respect to $\Delta \bar{P}_e(k)$. This method improves the MPPT performance by solving the slow response and high fluctuations near maximum power points.

B. POWER CURTAILMENT CONTROL

The PTO control force from (55) generates uncontrolled power that depends on sea state conditions rather than a defined power reference. Calculating a PTO control force that enables power following is not straightforward as it complicates the control design due to additional computational requirements such as excitation force predictions and real-time optimization solvers. However, it is noticed from (29) that scaling down the PTO control force can decrease the absorbed power and, consequently, the generated

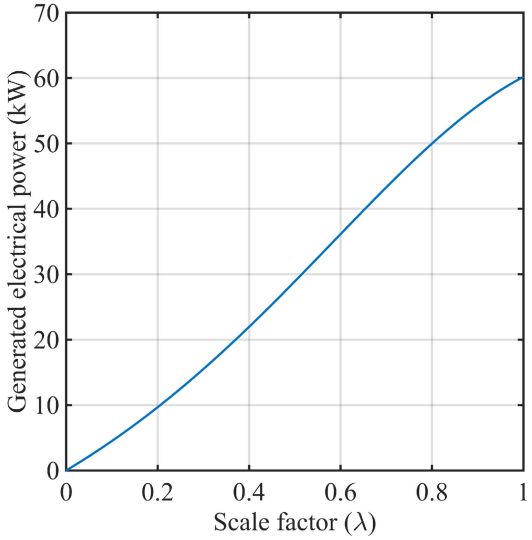

FIGURE 6. The WEC generated power subjected to scale factor variations.

power. Figure 6 shows the changes in mean generated power due to scaling down the PTO control force by different scale factors.

This work proposes a novel power tracking strategy that includes a PI controller to scale down the calculated MPPT control force to achieve a desired power setpoint. This PI controller, called the power curtailment controller (PCC), aims to reduce power generation.The use of PI controllers for this power tracking control strategy provides several benefits including computational simplicity and the capability for manual tuning the PI parameters without requiring in-depth knowledge of the WEC model. Additionally, the PCC controller operates at a slower rate compared to the PI controllers in the lower-level current control loop, discussed in Subsection IIIc. This difference in rates enhances the overall system stability by enabling each PI controller to concentrate on its specific objective with minimum interference among them [55]. Finally, the proportional action provides a responsive adjustment to changes in the running mean generated power, while the integral action corrects any cumulative errors.

The PI controller receives the mean generated power and compares it with the power setpoint to determine the proper scale factor given by the following:

$$\lambda(t) = K_{pp}\left(P_e^*(t) - \bar{P}_e(t)\right) + K_{ip}\int_0^t \left(P_e^*(\tau) - \bar{P}_e(\tau)\right) d\tau \tag{58}$$

where λ and P_e^* are the scale factor and power setpoint, respectively. The proportional gain is denoted by K_{pp}, whereas K_{ip} is the integral gain. The scale factor λ is bounded by the range $[0,\ 1]$. To ensure faster dynamics and performance, the control rate of the PI controller should be faster than the MPPT's control rate. The scaling factor is multiplied by the MPPT control force to obtain the modified control force for power following as follows:

$$f_u^{pc}(t) = \lambda(t) \cdot f_u^{mppt}(t). \tag{59}$$

The MPPT reactive control and PI-based PCC are both integrated in the upper-level control, as shown in Fig. 7, to govern the power output of the heaving WEC by defining the PTO control force reference as follows:

$$f_u^*(t) = \begin{cases} f_u^{mppt}(t) \text{ for max. power generation} \\ f_u^{pc}(t) \quad \text{for power setpoint following.} \end{cases} \tag{60}$$

The advantages of this proposed control strategy revolve around its simplicity and the low computational requirement to shift between maximum power generation and power command tracking alternatively. The strategy is less susceptible to model errors and uncertainty because it adopts a model-free approach that does not need excitation force predictions. Furthermore, only measurements of the heave displacement, heave velocity, and PMLG-generated power are required, which are easily obtained from commercialized sensors from the market. In addition, the absence of an optimization problem eases the restrictions for real-time operations. Finally, the PI PCC does not affect how the MPPT calculates its control force. Thus, it can be simply integrated into any maximum power absorption control strategy.

C. LOWER-LEVEL CURRENT CONTROL

The lower-level current control, shown in Fig. 8, realizes the PTO-controlled force reference $f_u^*(t)$ received from the upper-level control. This is often accomplished by changing the PMLG stator currents in real-time via AC/DC converter. The PMLG can be modeled with the AC/DC converter by expressing $v_{sd}(t)$ and $v_{sq}(t)$ in terms of converter control actions as follows:

$$v_{sd}(t) = v_{dc}u_{sd}(t) \tag{61}$$

$$v_{sq}(t) = v_{dc}u_{sq}(t) \tag{62}$$

where $u_{sd}(t)$ and $u_{sq}(t)$ represent the d-q components of the control signal for the rectifier switches expressed by the

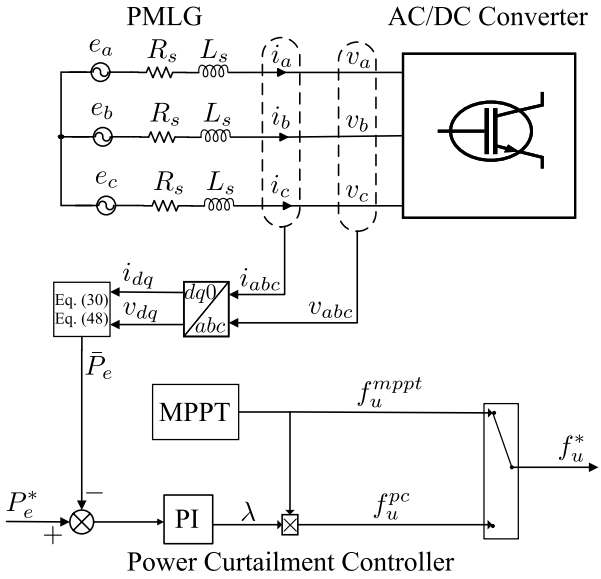

FIGURE 7. The upper-level current structure.

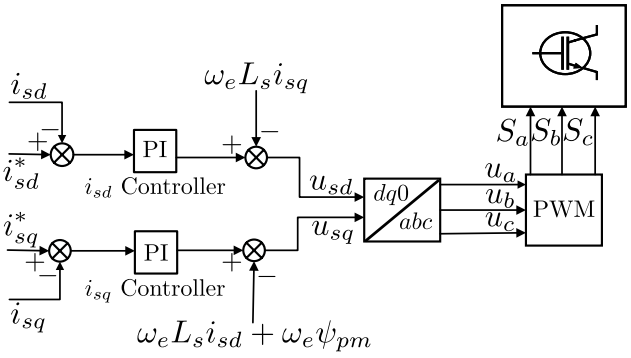

FIGURE 8. The lower-level current structure.

following:

$$S_i = \begin{cases} 1 & \text{if } S_i \text{ is ON and } S_i' \text{ is OFF} \\ 0 & \text{if } S_i \text{ is OFF and } S_i' \text{ is ON} \end{cases} \quad i = a, b, c \tag{63}$$

by substituting the values of $v_{sd}(t)$ and $v_{sq}(t)$ from (61) and (62) into (26) and (27), the PTO model becomes the following:

$$\frac{di_{sd}(t)}{dt} = \frac{-R_s i_{sd}(t)}{L_s} + \omega_e(t) i_{sq}(t) - \frac{v_{dc} u_{sd}(t)}{L_s} \tag{64}$$

$$\frac{di_{sq}(t)}{dt} = \frac{-R_s i_{sq}(t)}{L_s} + \omega_e(t) i_{sd}(t) - \frac{\omega_e(t)}{L_s}\phi_{pm} - \frac{v_{dc} u_{sq}(t)}{L_s} \tag{65}$$

The i_{sd} is controlled by v_{sd}, while the i_{sq} is controlled by the v_{sq}. The direct current reference i_{sd}^* is set to zero to reduce copper power loss, whereas the quadrature current reference i_{sq}^* is given from (28) as follows:

$$i_{sq}^*(t) = \frac{2\tau_p}{3\pi\phi_{pm}} f_u^*(t). \tag{66}$$

Two PI control loops are used to regulate the actual d-q component stator currents. To eliminate the cross-coupling terms shown in (64) and (65), feed-forward compensation is added to the PI controllers' output [55]. Finally, a sinusoidal pulse width modulation is used to generate the switching states for the AC/DC converter.

D. ENERGY STORAGE SYSTEM CONTROL

The objective of the ESS controller is to compensate for the voltage fluctuations in the DC bus, which are caused by imbalances between generated and consumed power. This control system adopts a two-cascaded loop structure, as shown in Fig. 9.

Voltage control is dealt with by the PI controller in the outer loop. The outer PI controller compares the measured DC voltage v_{dc} with the reference DC voltage v_{dc}^* to generate the supercapacitor current i_{sc}^* reference required in regulating the DC bus voltage. Given the voltage controller's proportional gain K_{po} and integral gain K_{io}, i_{sc}^* is calculated as follows:

$$i_{sc}^* = K_{po}\left(v_{dc}(t)^* - v_{dc}(t)\right) + K_{io}\int_0^t \left(v_{dc}(\tau)^* - v_{dc}(\tau)\right) d\tau \tag{67}$$

The inner PI controller receives i_{sc}^* and compares it with the measured supercapacitor current to generate the control signal u_{12}. The control signal is then transmitted to a pulse width modulation generator to produce the IGBT switches for the DC/DC converter. Given the current controller's proportional gain K_{pi} and integral gain K_{ii}, the control signal is expressed as follows:

$$u_{12} = K_{pi}\left(i_{sc}(t)^* - i_{sc}(t)\right) + K_{ii}\int_0^t \left(i_{sc}(\tau)^* - i_{sc}(\tau)\right) d\tau \tag{68}$$

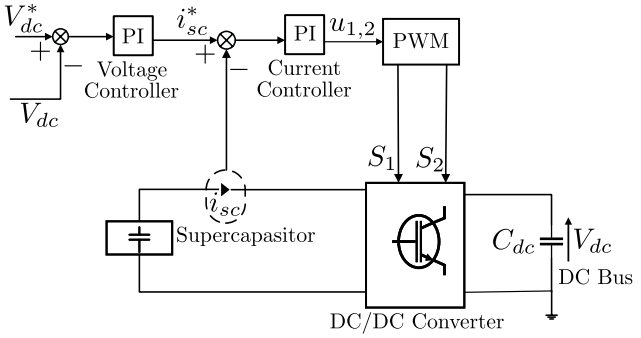

FIGURE 9. Supercapacitor energy storage control structure.

TABLE 1. WEC system parameters.

Parameter	Symbol (value)
Buoy diameter	D (5 m)
Total mass	m (3×10^4 kg)
Buoy added mass at infinite frequency	m_∞ (2.85×10^4 kg)
Buoy surface area	A_w (19.6 m^2)
Buoyancy stiffness coeficient	C_b (1.9×10^2 N/m)
Restoring spring stiffness coeficient	C_{rs} (6×10^4 N/m)
Sea water density	ρ (1.025×10^3 kg/m^3)
Gravitational acceleration	g (9.8 m/s^2)
PMLG flux linkage	ϕ_{pm}(19.8 Wb)
PMLG pole pitch	τ_p (4.5×10^{-2} m)
Number of turns per-phase	N_p (550)
PMLG stator resistance	R_s (5 Ω)
PMLG stator inductance	L_s (32 mH)
DC bus capacitor	C_{dc} (2.7 mF)
Supercapacitor resistance	R_{sc} (30 mΩ)
Supercapacitor capacitance	C_{sc} (11 F)
DC/DC Inductor	L_{sc} (3.3 mH)
Supercapacitor rated voltage	v_{sc} (700 V)
DC resistive load	R_l (50 Ω)

IV. RESULTS AND DISCUSSION

A. HARDWARE-IN-THE-LOOP EXPERIMENTAL SETUP

An experiment is conducted to evaluate the heaving WEC's performance under maximum power generation and power setpoint tracking. Given the complexity of deploying an actual WEC at sea, the hardware-in-the-loop (HIL) scheme was designed to replace the actual WEC with a virtual simulated model, similar with the structure of the HIL in [12]. Computer simulations of sea wave profiles, buoy hydrodynamics, PMLG, and supercapacitor energy storage are implemented in a MATLAB environment based on the mathematical models in section II. Furthermore, the HIL incorporates physical hardware devices to realize the control actions and validate its practicability in real-time applications. Finally, a dSPACE Micro Auto box system performs three primary tasks:

1) Run the WEC model in real-time and send the output power values to the programmable sources to produce.

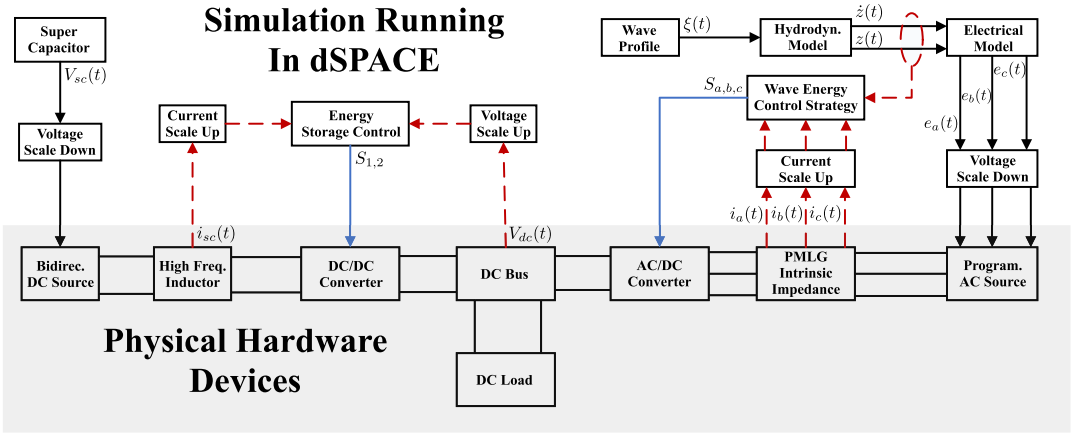

FIGURE 10. The schematic diagram of the HIL experimental setup.

TABLE 2. Physical hardware used in the HIL experimental setup.

Hardware description	Manufacturer (model)
DSP and control hardware	DSpace (1011/1013)
AC power source	Chroma (65107)
DC power source	Chroma (62060D)
AC/DC power converter	Taraz (SPM-VFD-MOS)
DC/DC power converter	Taraz (SPM-HB-MOS)
Three-phase resistor	Terco (MV 1100)
DC resistive load	Terco (MV 1961)
DC bus capacitor	Nichicon (81V32L-09)
Inductor	Inverpower (Reactor 10 A max)
High frequency inductor	SPM (9944)
Voltage & current trans.	Taraz (USM-3IV)

2) Feedback sensor measurements to the controller.
3) Send the switching states to the power converter.

Table 1 summarizes the WEC parameters used in this study. The physical hardware devices used in the HIL scheme are listed in Table 2. A schematic diagram and physical configuration of the HIL setup are shown in Fig. 10 and Fig. 11, respectively.

While the proposed controllers can be validated via computer simulation due to low computational requirements for real-time applications, using the dSPACE Micro Auto box for HIL testing offers key advantages. It enables real hardware interaction, such as using power converters for current regulation. This process can uncover issues related to pulse width modulation techniques for switching signal generation, which might not be evident in a purely simulated environment. Moreover, validating controllers in dSPACE ensures their robustness in real-world scenarios, especially against challenges like electrical noise from sensor measurements. Finally, this HIL configuration will be a platform to evaluate advanced computational control strategies for real-time implementation.

The MATLAB simulation part of the experimental setup runs at a sample period of 1×10^{-4} seconds. The MATLAB software simulates sea state profiles that produce wave

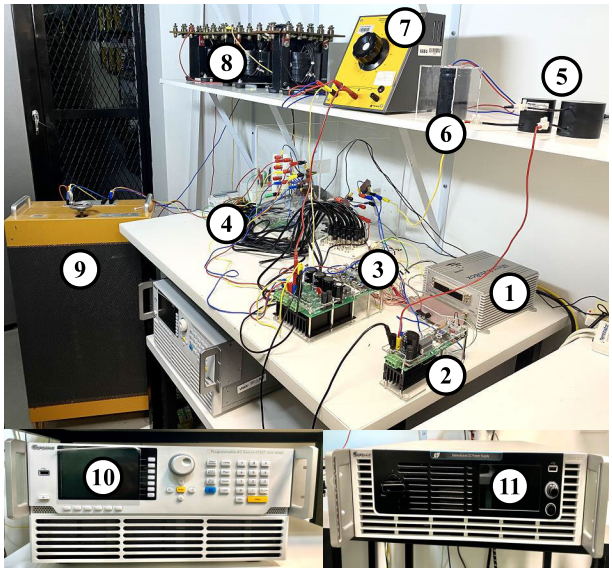

FIGURE 11. A physical configuration of the HIL experimental setup: (1) dSPACE board, (2) DC/DC converter, (3) AC/DC converter, (4) Voltage and current transducers, (5) High frequency inductor, (6) DC bus capacitor, (7) DC resistive load, (8) inductors, (9) three-phase resistors, (10) Programmable AC power source, (11) DC power source.

elevations to excite the WEC model. The resulted EMF voltages was implemented using the AC Programmable source. Since the actual voltages were too high to be generated by the programmable AC source, they were scaled down by a factor of 0.05. Output voltages of the AC source cause current to flow through physically connected resistors and inductors equal to the PMLG stator resistance and inductance. These currents resemble the scaled-down PMLG stator currents and can be controlled by the AC/DC power converter. To reinstate the PTO control force, the sensing currents are scaled up by a factor of 30 and sent to the WEC model in the MATLAB environment. The same method is adopted for energy storage, where the output voltage of the simulated supercapacitor is scaled down by a factor of

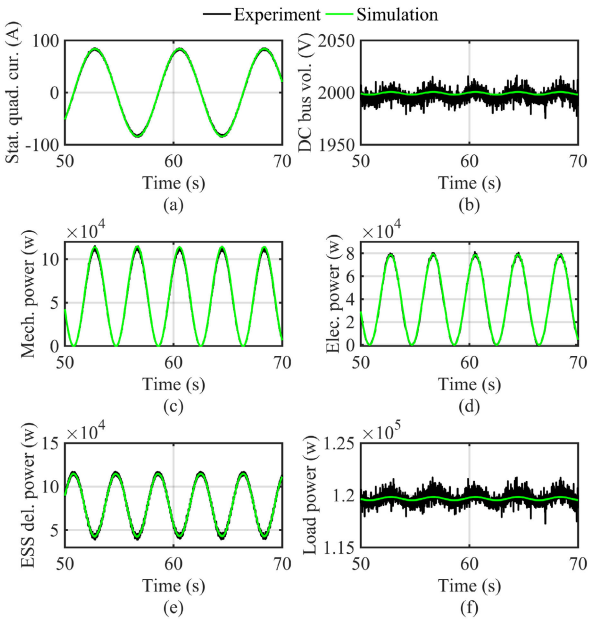

FIGURE 12. Comparison between simulation and experimental results with a monochromatic wave, where $H_s = 3$ m and $T_e = 8$ sec, in terms of: (a) stator quadrature current, (b) the voltage at the DC bus, (c) instantaneous absorbed mechanical power, (d) instantaneous generated power, (e) the power provided by the supercapacitor ESS, (f) the power across the DC load.

0.05 and sent to the DC power supply for generation. The output terminals of the DC power supply were connected physically to a high-frequency inductor and DC/DC power converter. The current flowing through the inductor and the DC bus voltage was scaled up by factors of 30 and 20, respectively, before being sent as feedback to the energy storage controller. Real-time measurements of currents and terminal output voltages are taken via V-I sensors and the dSPACE.

To validate the HIL scheme, experimental results are evaluated with simulation-based results in Fig. 12. The heaving WEC is assumed to be excited by a monochromatic sea state with $H_s = 3$ m and $T_e = 8$ sec and the damping control was chosen as the energy extraction algorithm. For the experimental results, voltage and current readings taken from actual sensor measurements are scaled by a factor of 20 and 30, respectively, to accommodate the scaling-down process caused by physical hardware limitations. It is apparent from Fig. 12 that there are minor discrepancies between the simulation and experimental results. Figure 12a demonstrates that using the Parke-Clarke transformation on three-phase stator currents in a monochromatic wave, marked by a varying frequency and magnitude AC pattern, leads to a sinusoidal quadrature stator. From Fig. 12c, the absorbed mechanical power is always positive, indicating a unidirectional power flow. When the generated power in Fig. 12d increases, the ESS delivered power in Fig. 12e decreases, and vice versa. This shows the ESS and its associated controller were able to stabilize the DC bus voltage and the power across the load, as shown in Fig. 12b and Fig. 12f, respectively.

TABLE 3. MPPT reactive control parameters.

Parameter	Symbol	Value
Control period	$T_{control}$	40 s
Fixed step-size	μ_{fixed}	2.5×10^4
Initial damping coefficient	$B_{pto}(0)$	8×10^4 Ns/m
Initial stiffness coefficient	$K_{pto}(0)$	5×10^4 N/m
Maximum damping coefficient	B_{pto}^{max}	3×10^4 Ns/m
Maximum stiffness coefficient	K_{pto}^{max}	2.5×10^4 N/m
Power difference threshold	P	10 kW

B. MAXIMUM POWER GENERATION

The control algorithm is applied to the HIL experimental setup to evaluate the proposed MPPT reactive control for maximum power generation. The MATLAB environment operates at a sampling period of 10 ms, and the design parameters of the MPPT reactive control are shown in Table 3. The controller is subjected to both monochromatic and polychromatic wave conditions. The monochromatic wave is of a wave period of $T = 9.4$ s and wave height of $H = 3.66$ m. It is employed to facilitate a more straightforward analysis of the MPPT performance, devoid of the intricacies posed by fluctuating wave conditions. This approach is vital for the initial validation of the control strategy's effectiveness in a consistent and repeatable environment. Meanwhile, the polychromatic wave with $T_e = 9.4$ s and $H_s = 3.66$ m is used to evaluate the MPPT performance under realistic sea conditions. Figure 13 depicts the difference between the monochromatic and polychromatic waves.

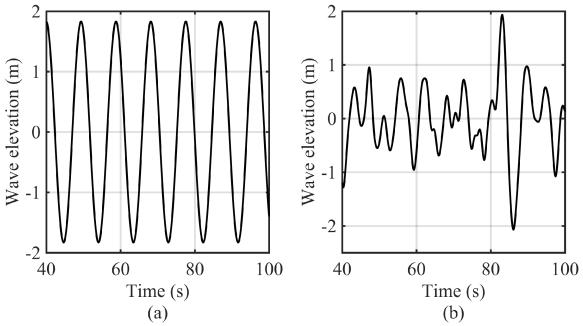

FIGURE 13. Sea surface elevation: (a) Monochromatic wave profile with $H = 3.66$ m and $T = 9.4$ s, (b) Polychromatic wave profile with $H_s = 3.66$ m and $T_e = 9.4$ s.

Figure 14 displays the efficacy of the MPPT reactive control under the monochromatic wave, depicted in Fig. 13a, for an extended duration of 600 s. The initial value of mean power was zero, while the initial values of both damping and stiffness coefficients were shown in Table 3. During every control period, the instantaneous generated electrical power was measured and its mean was calculated for the subsequent control period. It can be observed that the system started from

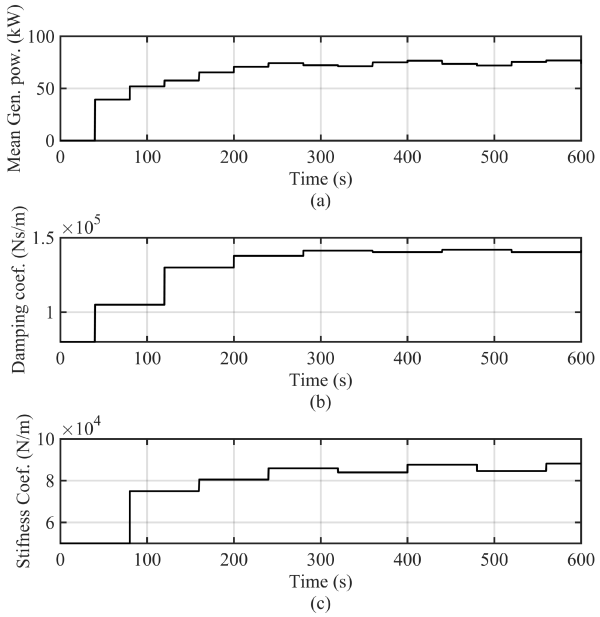

FIGURE 14. Experimental results of MPPT reactive control performance under monochromatic sea state 3: (a) mean generated electrical power, (b) damping coefficient B_{pto}, (c) stiffness coefficient K_{pto}.

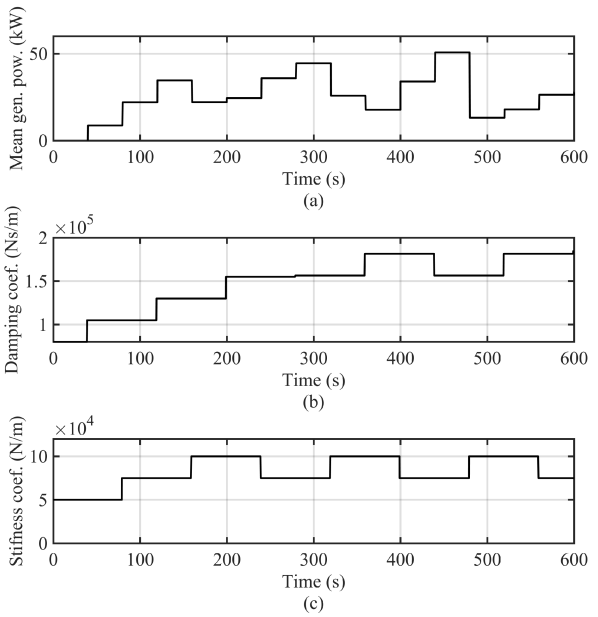

FIGURE 15. Experimental results of MPPT reactive control performance under polychromatic sea state 3: (a) mean generated electrical power, (b) damping coefficient B_{pto}, (c) stiffness coefficient K_{pto}.

a non-maximum power point and the coefficients increased with large step sizes due to large mean power deviations, and suddenly decreased as power deviations fall below the power difference threshold. After 280 s, the WEC approached its maximum power point, i.e., about 74.3 kW, and then oscillates slightly around that value as the coefficients slightly converge to their respective optimal values. At 240 s, K_{pto} increased from 8.04×10^4 N/m to 8.59×10^4 N/m resulting in a mean power decrease from 74,3 kW to 72.3 kW as seen at 280 s. The MPPT algorithm responded by decreasing K_{pto} to 8.37×10^4 N/m at 320 s. The same was noticed when B_{pto} increased from 1.37×10^5 Ns/m to 1.41×10^5 Ns/m at 280 s, which decreased the mean power to 71.2 kW as seen at 320 s. The MPPT acted by increasing B_{pto} to 1.40×10^5 Ns/m at 360 s. These responses prove that the MPPT updates both coefficients in the direction that leads to maximum power. Minor oscillations in these values were observed due to slight variations in the mean generated power between control periods, arising from the fixed periods capturing different portions of the wave cycle. This leads to inconsistent power extraction, caused by phase misalignment and the asymmetric distribution of power across the wave cycle.

Figure 15 depicts the MPPT reactive control behavior when exposed to the polychromatic wave conditions, as presented in Fig. 13b. Similar to the monochromatic condition, the coefficients were assigned with their respective initial values, as depicted in Fig. 15b and Fig. 15c, and the MPPT perturbed them based on the mean power measurements. However, the fluctuations in polychromatic waves lead to notable power deviations, as depicted by the mean generated power in Figure 15a. This is particularly evident at 480 s, where there was a significant decline in the mean power from 50.71 kW to 13.16 kW. The damping coefficient, B_{pto}, demonstrated a progressive rise as the power increases, culminating at the peak of 1.81×10^5 Ns/m. Subsequently, there was a decreasing to 1.56×10^5 Ns/m at 440 s, corresponding with a decline in the mean power output from 25.8 kW to 17.7 kW at 360 s, before it ascended again to 1.81×10^5 Ns/m. Meanwhile, K_{pto} increased as the power increased until reaching 1×10^5 N/m at 160 s. For the remaining duration, the K_{pto} alternated between 1×10^5 N/m and 7.5×10^4 N/m depending on the rise or drop in the mean generated power. It is evident that the power variations measured at each sampling period exceeded the set power difference threshold, leading to larger step changes in the coefficient updates. However, an exception occurred at 280 s when the value of B_{pto} increased by 1491, a modification attributed to the mean generated power witnessing an increment of 1.56 kW at 200 s.

Several points of concern emerge regarding the performance of the MPPT reactive control under polychromatic waves. Despite offering a simple and cost-effective method for adjusting the damping and stiffness coefficients, the intrinsic variability of polychromatic waves impedes the MPPT's capability to converge the coefficient values, such as in monochromatic conditions. This challenge arises because the MPPT struggles to determine whether shifts in power output stem from changes in coefficients or from the inherent fluctuations in wave power. Furthermore, the presence of two tuning variables complicates the process of tracking maximum power. Finally, while large control periods are necessary to provide sufficient power information, they delay

TABLE 4. Applied sea-states and their characteristics.

Param., sym. (unit)	S1	S2	S3	S4	S5
Sign. height, H_s (m)	1.52	3.09	3.66	5.18	7.43
Energy period, T_e (s)	6.4	7.8	9.4	10.1	12.3
Mono. pow., $\bar{P}_w$ (kW)	72.6	365.4	723.8	1329.6	3331.3
Poly. pow., $\bar{P}_w$ (kW)	36.3	182.7	361.9	664.8	1665.7

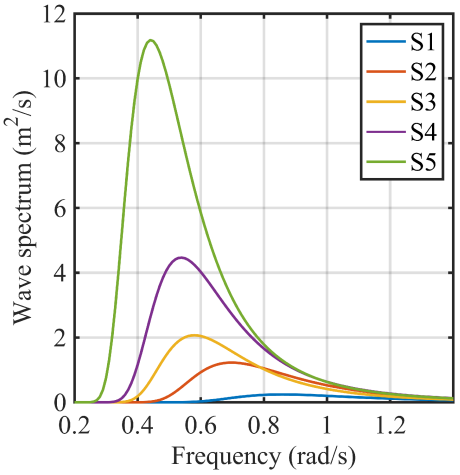

FIGURE 16. Wave energy spectrum based on different sea-states characteristics.

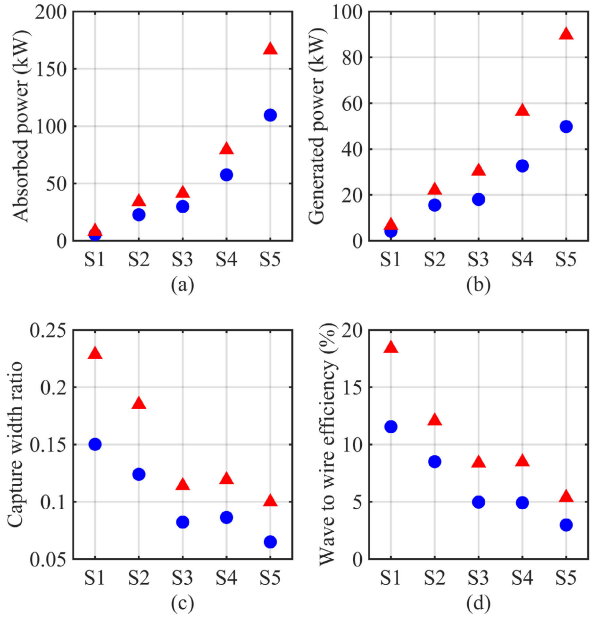

FIGURE 17. Comparison between damping control (blue circle) and MPPT reactive control (red triangle) in terms of: (a) average mechanical absorbed power, (b) average generated electrical power, (c) capture width ratio, (d) wave to wire efficiency.

the MPPT response, as counteractive coefficient updates are performed in the subsequent control period.

Furthermore, technical assessments are conducted to evaluate the proposed MPPT reactive control strategy against damping control. These technical assessments include

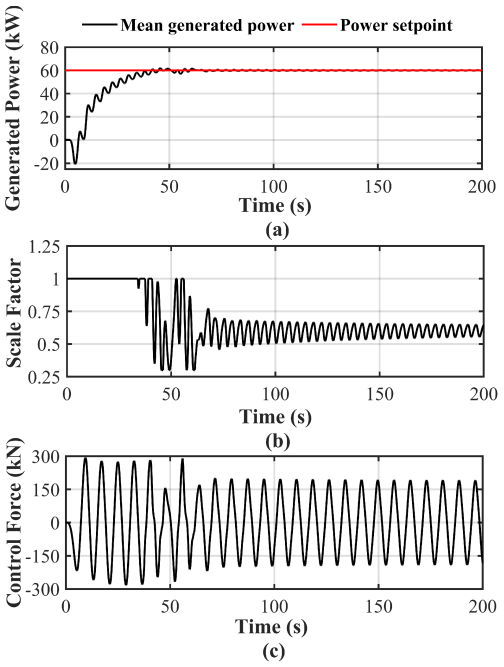

FIGURE 18. The power tracking performance of the power curtailment controller under a monochromatic wave: (a) running mean generated power, (b) scale factor, (c) PTO control force.

mechanical absorbed power, generated electrical power, capture width ratio (CWR) and the wave to wire efficiency (η_{w2w}). The capture width ratio is a dimensionless assessment that describes the WEC's ability to absorb wave energy, whereas the wave-to-wire efficiency describes the WEC's efficiency in converting wave power into electrical generated power. The following equations calculate both assessments

$$CWR = \frac{\bar{P}_m}{\bar{P}_w \cdot D} \tag{69}$$

$$\eta_{w2w} = \frac{\bar{P}_e}{\bar{P}_w \cdot D} \times 100\% \tag{70}$$

where

$$\bar{P}_m = \frac{1}{N_s} \sum_{i=0}^{N_s} P_m(i). \tag{71}$$

Polychromatic sea wave profiles containing five sea states with varying energy periods T_e and significant wave height H_s, were applied to investigate the technical assessments under different wave conditions. The polychromatic wave profiles were modeled using the PM wave spectrum, and Table 4 illustrates the characteristics of the applied sea states, whereas Fig. 16 shows their respective wave energy spectrum. It is noticed from Fig. 16 that S1 and S5 contain the lowest and the highest available energy, respectively.

Fig. 17 presents a comparative analysis between the MPPT reactive control and the damping control strategies under polychromatic sea conditions detailed in Table 4. Both control strategies run for a duration of 1000 s and compared

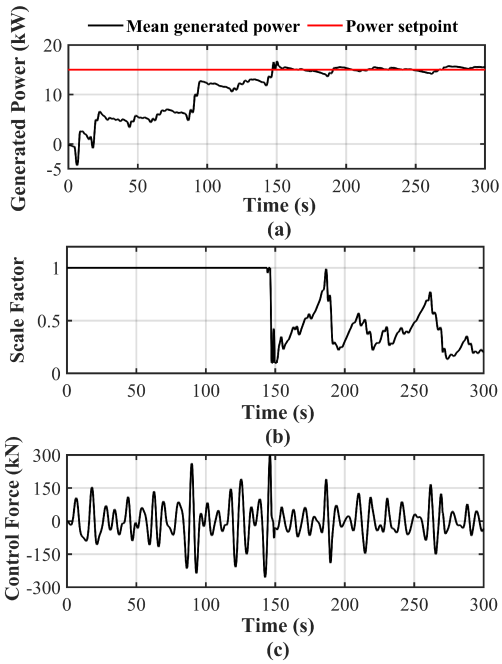

FIGURE 19. The power tracking performance of the power curtailment controller under a polychromatic wave: (a) running mean generated power, (b) scale factor, (c) PTO control force.

on the basis of average mechanical absorbed power, average generated electrical power, capture width ratio (CWR) and the wave to wire efficiency ((η_{w2w})). It's obviously seen that the MPPT shows greater superiority in all the assessments. The MPPT achieves an average absorbed power of 8.29 kW, 33.92 kW, 41.25 kW, 79.3 kW, and 166 kW in sea-states 1, 2, 3, 4, and 5, respectively. This shows an increase ranging from 65% to 72% when compared to damping control. The same is noticed in Fig. 17b, where the MPPT increased the WEC power generation by 62.5%, 70.6%, 59.4%, 57.9% and 55.4% sea state 1, 2, 3, 4 and 5, respectively. Furthermore, the overall capture width ratio for the MPPT varies between 0.22 and 0.1, which is greater than that of damping control, i.e., 0.065−0.15 as shown in Fig. 17c. However, they both exhibit similarities in which they both decrease in more energetic wave profiles, which is intuitive considering that greater wave power is available. This is because WECs have amplitude restrictions caused by the finite buoy volume, or by limits on the stroke of the PMLG [3]. From Fig. 17d, lower wave to wire efficiency η_{w2w} were also recorded for more energetic sea states due to the amplitude restrictions and that larger control forces f_u are required, resulting in higher PMLG stator currents and hence greater copper losses.

C. POWER SETPOINT FOLLOWING

The power curtailment controller is activated when the heaving WEC operates at power setpoint following mode. The PI controller runs at a sampling period of 0.01 s, and the scaling factor λ is bounded by the range [0.1, 1]. Figure 18 depicts the effectiveness of the power curtailment controller

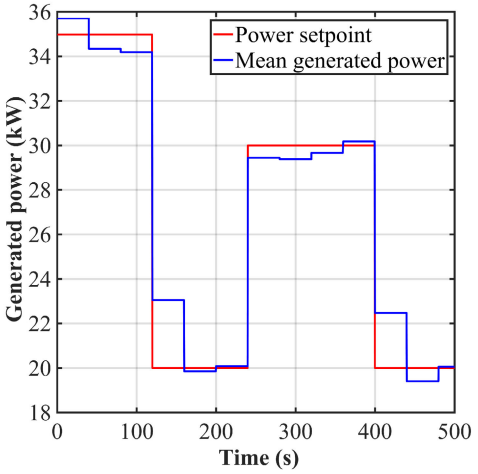

FIGURE 20. Power setpoint following performance of a heaving WEC under a monochromatic sea-state.

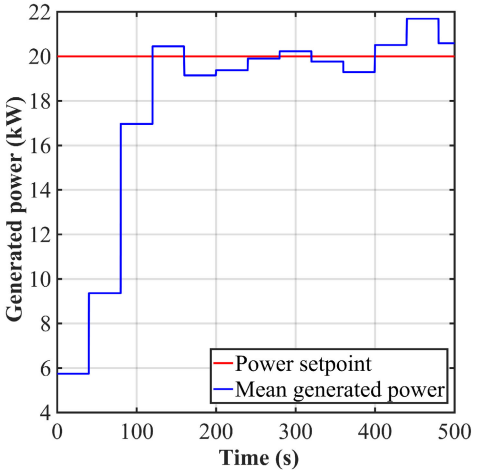

FIGURE 21. Power setpoint following performance of a heaving WEC under a polychromatic sea-state.

in tracking power under a monochromatic wave is depicted. This wave has wave height of 3 m coupled with a wave period of 8 s. The heaving WEC managed to follow the desired power setpoint of 60 kW, as seen in Fig. 18a. Figure 18b illustrates the relation between the scale factor λ and the running mean generated power $\bar{P}_e$. Initially, λ operates at its maximum, a value of 1. This continues until the 36.4 s, at which point $\bar{P}_e$ aligns with its power setpoint, prompting a variation in λ. Whenever $\bar{P}_e$ is below the power setpoint, λ increases, and vice versa. After 75.5 s, the controller managed to confine $\bar{P}_e$ close to the power setpoint. It is seen from Fig. 18c that λ effects the control force magnitude in a proportional relation.

Figure 19 shows the power tracking performance under polychromatic wave with $H_s = 3$ m and $T_e = 8$ s. The controller is tasked with following a power setpoint of 60 kW. During the initial 150 seconds, the WEC operates at its peak generation capacity to attain the specified power command.

This is shown by $\lambda = 1$, as illustrated in Fig. 19b. Similar to the monochromatic wave condition, when $\bar{P}_e$ lingers beneath the power setpoint, there's a consequent increase in λ, and the opposite occurs when the power exceeds the setpoint. However, λ convergence is not seen because of the rapid power variations in polychromatic wave conditions. This suggests that as the wave power content increases, λ experiences a decrement, and vice versa.

Figures 20 and 21 demonstrate the efficacy of the PCC strategy for the heaving WEC in relation to power setpoints. This is illustrated under two separate wave scenarios: monochromatic waves, as shown in Fig. 20, and polychromatic waves, as presented in Fig. 21. The wave characteristics align with those depicted in Fig. 13, and the instantaneous generated power is averaged every 40 s, akin to the methodology employed for recording the generated power in the MPPT reactive control. In Fig. 20, the power setpoint varies every 120 s, starting with 35 kW and changes to 20 kW than 30 kW and finally 20 kW. Contrasting with the maximum power generation depicted in Fig. 14a, the WEC generates power at levels below its maximal capacity, approximately 74.3 kW, in order to comply with the predetermined power setpoints. Furthermore, it's noticed that some transient time is required for the WEC to remain within suitable ranges around the power setpoint, as this duration facilitates the convergence of the scale factor λ.

In Fig. 21, a constant power of 20 kW was given as the power setpoint. At the start, the mean generated power was below the required setpoint, and hence maximum power generation mode is activated and the MPPT Reactive control algorithm tuned the coefficients until the setpoint is reached at 120 s. After 120 s, the active power PI controller managed to regulate the generated output at a range between 19.1 kW and 21.69 kW because of the fluctuating power contents in polychromatic sea states.

V. CONCLUSION

In this paper, the control issue for a heaving WEC operating at maximum power generation or power setpoint following is addressed. Maximum power generation is achieved through a reactive control strategy employing a variable step size MPPT algorithm. This algorithm tunes the damping and stiffness coefficients toward maximum power generation, which dictates the control force. The MPPT algorithm is a low computational approach that is less susceptible to WEC uncertainties and avoids the need for wave frequency knowledge. The results from the HIL experimental setup demonstrated that in the case of monochromatic wave conditions, the MPPT reactive control effectively modified the coefficients. This adjustment continued until a convergence was achieved at values that maximize power generation. Then, the controller was subjected to a polychromatic wave to assess its performance in real sea wave environments. It was noticed that the intrinsic variability of polychromatic waves caused the MPPT to continuously adjust the coefficients, thus preventing a convergence such as in monochromatic conditions. Furthermore, a comparative analysis was undertaken to evaluate the performance of the MPPT reactive control against damping control across various polychromatic sea states. The experimental findings indicated that the proposed control approach exhibited superior performance in a range of technical evaluations. Notably, it was able to generate an excess of 55.4% electrical power compared to the damping control for each polychromatic sea state.

For the power setpoint following, the control force, as determined by the MPPT algorithm, is multiplied by a scale factor determined by a PI-based PCC. The advantage of this strategy is that it will add flexibility to the WEC system, allowing it to function as a more controllable power source by regulating its generation phase power, thus reducing its reliance on an ESS. Furthermore, this strategy is independent of the control force computations derived from the MPPT. This characteristic facilitates its seamless incorporation into other methods to maximize power absorption. Results show the efficiency of the PCC, where decreasing the scale factor reduces the magnitude of the control force, thus limiting the generation output of the WEC to levels beneath its maximum capacity to track predefined power commands accurately. This efficiency was particularly notable in monochromatic wave conditions because the uniform nature of these waves facilitated a more straightforward scale factor determination. The irregularities in polychromatic waves introduced difficulties for the PPC, yet it managed to maintain the power output within satisfactory limits near the power reference.

Future research work of this study may involve incorporating artificial intelligence and machine learning techniques to forecast the varying wave conditions and adapt the parameters of the MPPT algorithm accordingly. This incorporation aims to allow the MPPT algorithm to differentiate between changes in power output caused by coefficient modifications and those resulting from fluctuations in wave energy. Regarding the PCC strategy, proper tuning of the PI controller presents a significant challenge due to the fluctuating power content of polychromatic waves. Improper tuning can lead to potential issues like slow response and oscillations if not properly calibrated. Thus, an adaptive method is preferred to automatically tune the gains in accordance with the prevailing wave conditions. Finally, an energy management strategy is needed to shift between maximum generation and setpoint following. This guarantees that power generation remains within the limits of what the interconnected power system can absorb and the ESS's storage capacity, ensuring optimal utilization.

REFERENCES

[1] H. E. Murdoch, "Renewable 2020-global status report," Renew. Energy Policy Netw. 21st Century (REN21), 2020. [Online]. Available: http://www. Ren21.net/gsr-2020/

[2] F. Taveira-Pinto, G. Iglesias, P. Rosa-Santos, and Z. D. Deng, *Preface to Special Topic: Marine Renewable Energy*. New York, NY, USA: AIP Publishing, 2015.

[3] M. E. McCormick, *Ocean Wave Energy Conversion*. Wiley, 1981.

[4] K. Budar and J. Falnes, "A resonant point absorber of ocean-wave power," *Nature*, vol. 256, no. 5517, pp. 478–479, Aug. 1975.
[5] S. Zheng, G. Zhu, D. Simmonds, D. Greaves, and G. Iglesias, "Wave power extraction from a tubular structure integrated oscillating water column," *Renew. Energy*, vol. 150, pp. 342–355, May 2020.
[6] E. Kasiulis, P. Punys, and J. P. Kofoed, "Assessment of theoretical near-shore wave power potential along the Lithuanian coast of the Baltic sea," *Renew. Sustain. Energy Rev.*, vol. 41, pp. 134–142, Jan. 2015.
[7] L. Wang, J. Isberg, and E. Tedeschi, "Review of control strategies for wave energy conversion systems and their validation: The wave-to-wire approach," *Renew. Sustain. Energy Rev.*, vol. 81, pp. 366–379, Jan. 2018.
[8] D. Clemente, P. Rosa-Santos, and F. Taveira-Pinto, "On the potential synergies and applications of wave energy converters: A review," *Renew. Sustain. Energy Rev.*, vol. 135, Jan. 2021, Art. no. 110162.
[9] S. R. Sinsel, R. L. Riemke, and V. H. Hoffmann, "Challenges and solution technologies for the integration of variable renewable energy sources—A review," *Renew. Energy*, vol. 145, pp. 2271–2285, Jan. 2020.
[10] C. Byers, T. Levin, and A. Botterud, "Capacity market design and renewable energy: Performance incentives, qualifying capacity, and demand curves," *Electr. J.*, vol. 31, no. 1, pp. 65–74, Jan. 2018.
[11] M. Cepeda and D. Finon, "Generation capacity adequacy in interdependent electricity markets," *Energy Policy*, vol. 39, no. 6, pp. 3128–3143, Jun. 2011.
[12] J. Falnes, "A review of wave-energy extraction," *Mar. Struct.*, vol. 20, no. 4, pp. 185–201, Oct. 2007.
[13] A. Maria-Arenas, A. J. Garrido, E. Rusu, and I. Garrido, "Control strategies applied to wave energy converters: State of the art," *Energies*, vol. 12, no. 16, p. 3115, Aug. 2019.
[14] D. Son and R. W. Yeung, "Real-time implementation and validation of optimal damping control for a permanent-magnet linear generator in wave energy extraction," *Appl. Energy*, vol. 208, pp. 571–579, Dec. 2017.
[15] A. Wahyudie and M. A. Jama, "Perspectives on damping strategy for heaving wave energy converters," *IEEE Access*, vol. 5, pp. 22224–22233, 2017.
[16] J. Falnes amd A. Kurniawan, *Ocean Waves and Oscillating Systems: Linear Interactions Including Wave-Energy Extraction*. Cambridge, U.K.: Cambridge Univ. Press, 2020.
[17] A. Wahyudie, O. Saeed, M. Jama, H. Noura, and K. Harib, "Maximising power conversion for heaving point absorbers using a reference-based control technique," *IET Renew. Power Gener.*, vol. 11, no. 3, pp. 271–280, Feb. 2017.
[18] E. Anderlini, D. I. M. Forehand, E. Bannon, Q. Xiao, and M. Abusara, "Reactive control of a two-body point absorber using reinforcement learning," *Ocean Eng.*, vol. 148, pp. 650–658, Jan. 2018.
[19] E. A. Amon, T. K. A. Brekken, and A. A. Schacher, "Maximum power point tracking for ocean wave energy conversion," *IEEE Trans. Ind. Appl.*, vol. 48, no. 3, pp. 1079–1086, May 2012.
[20] M. Jama and A. Wahyudie, "Online damping strategy for controlling heaving wave energy converters using three-phase bridge boost rectifier," *IEEE Access*, vol. 5, pp. 7682–7691, 2017.
[21] B. F. Mon, A. Wahyudie, M. A. Jama, S. Akbar, S. Mekhilef, H. Shareef, K. Harib, and R. Errouissi, "Assessment of damping control using maximum power point tracking methods for heaving wave energy converters," *IEEE Access*, vol. 9, pp. 168907–168921, 2021.
[22] X. Xiao, X. Huang, and Q. Kang, "A hill-climbing-method-based maximum-power-point-tracking strategy for direct-drive wave energy converters," *IEEE Trans. Ind. Electron.*, vol. 63, no. 1, pp. 257–267, Jan. 2016.
[23] E. Anderlini, D. I. M. Forehand, E. Bannon, and M. Abusara, "Reactive control of a wave energy converter using artificial neural networks," *Int. J. Mar. Energy*, vol. 19, pp. 207–220, Sep. 2017.
[24] M. Jama, A. Assi, A. Wahyudie, and H. Noura, "Self-tunable fuzzy logic controller for the optimization of heaving wave energy converters," in *Proc. Int. Conf. Renew. Energy Res. Appl. (ICRERA)*, Nov. 2012, pp. 1–6.
[25] M. Jama, A. Wahyudie, A. Assi, and H. Noura, "Controlling heaving wave energy converter using function-based model predictive control technique," in *Proc. 25th Chin. Control Decis. Conf. (CCDC)*, May 2013, pp. 2705–2710.
[26] R. G. Coe, G. Bacelli, D. G. Wilson, O. Abdelkhalik, U. A. Korde, and R. D. Robinett III, "A comparison of control strategies for wave energy converters," *Int. J. Mar. Energy*, vol. 20, pp. 45–63, Dec. 2017.
[27] B. Ling and B. Batten, "Using extended Kalman filters for real-time estimation of excitation forces on a wave energy converter," in *Proc. 3rd Mar. Energy Technol. Symp.*, 2015, pp. 1–5.
[28] M. Jama, A. Wahyudie, and S. Mekhilef, "Wave excitation force estimation using an electrical-based extended Kalman filter for point absorber wave energy converters," *IEEE Access*, vol. 8, pp. 49823–49836, 2020.
[29] K. Mahmoodi, E. Nepomuceno, and A. Razminia, "Wave excitation force forecasting using neural networks," *Energy*, vol. 247, May 2022, Art. no. 123322.
[30] C. Boström, B. Ekergård, R. Waters, M. Eriksson, and M. Leijon, "Linear generator connected to a resonance-rectifier circuit," *IEEE J. Ocean. Eng.*, vol. 38, no. 2, pp. 255–262, Apr. 2013.
[31] O. Saeed, A. Wahyudie, T. B. Susilo, and H. Shareef, "Simple resonance circuit to improve electrical power conversion in a two-sided planar permanent magnet linear generator for wave energy converters," *IEEE Access*, vol. 5, pp. 18654–18664, 2017.
[32] N. Mararakanye and B. Bekker, "Renewable energy integration impacts within the context of generator type, penetration level and grid characteristics," *Renew. Sustain. Energy Rev.*, vol. 108, pp. 441–451, Jul. 2019.
[33] M. Blanco, G. Navarro, M. Lafoz, and J. Perez, "Study of the impact of wave energy generation in the frequency of an island electric grid," in *Proc. 12th Eur. Wave Tidal Energy Conf. (EWTEC)*, Dublin, Ireland, 2017.
[34] S. Rasool, K. M. Muttaqi, and D. Sutanto, "Modelling of a wave-to-wire system for a wave farm and its response analysis against power quality and grid codes," *Renew. Energy*, vol. 162, pp. 2041–2055, Dec. 2020.
[35] A. Blavette, D. L. O'Sullivan, A. W. Lewis, and M. G. Egan, "Impact of a wave farm on its local grid: Voltage limits, flicker level and power fluctuations," in *Proc. Oceans-Yeosu*, May 2012, pp. 1–9.
[36] T. Alazemi, M. Darwish, and M. Radi, "TSO/DSO coordination for RES integration: A systematic literature review," *Energies*, vol. 15, no. 19, p. 7312, Oct. 2022.
[37] S. Rasool, K. M. Muttaqi, and D. Sutanto, "A multi-filter based dynamic power sharing control for a hybrid energy storage system integrated to a wave energy converter for output power smoothing," *IEEE Trans. Sustain. Energy*, vol. 13, no. 3, pp. 1693–1706, Jul. 2022.
[38] S. Vazquez, S. M. Lukic, E. Galvan, L. G. Franquelo, and J. M. Carrasco, "Energy storage systems for transport and grid applications," *IEEE Trans. Ind. Electron.*, vol. 57, no. 12, pp. 3881–3895, Dec. 2010.
[39] Y. Li, X. Wang, X. Fang, Y. Liu, P. Zhao, and R. Cui, "Modeling and control strategy analysis of a hydraulic energy-storage wave energy conversion system," *Renew. Energy*, vol. 182, pp. 969–981, Jan. 2022.
[40] G. Brando, A. Dannier, A. Del Pizzo, L. P. Di Noia, and C. Pisani, "Grid connection of wave energy converter in heaving mode operation by supercapacitor storage technology," *IET Renew. Power Gener.*, vol. 10, no. 1, pp. 88–97, Jan. 2016.
[41] F. Meng, B. Ding, N. Y. Sergiienko, H. Chen, H. Xu, and Y. Li, "Power set-point tracking of a wave energy converter with multiple power take-off units in irregular waves," *IEEE Trans. Sustain. Energy*, vol. 13, no. 2, pp. 767–777, Apr. 2022.
[42] M. Yin, Y. Xu, C. Shen, J. Liu, Z. Y. Dong, and Y. Zou, "Turbine stability-constrained available wind power of variable speed wind turbines for active power control," *IEEE Trans. Power Syst.*, vol. 32, no. 3, pp. 2487–2488, May 2017.
[43] R. Subha and S. Himavathi, "Active power control of a photovoltaic system without energy storage using neural network-based estimator and modified P&O algorithm," *IET Gener., Transmiss. Distrib.*, vol. 12, no. 4, pp. 927–934, Feb. 2018.
[44] W. J. Pierson Jr., and L. Moskowitz, "A proposed spectral form for fully developed wind seas based on the similarity theory of SA Kitaigorodskii," *J. Geophys. Res.*, vol. 69, no. 24, pp. 5181–5190, 1964.
[45] K. Hasselmann, T. P. Barnett, E. Bouws, H. Carlson, D. E. Cartwright, K. Enke, J. A. Ewing, H. Gienapp, D. E. Hasselmann, P. Kruseman, A. Meerburg, P. Muller, D. J. Olbers, K. Richter, W. Sell, and H. Walden, "Measurement of wind-wave growth and swell decay during the joint north sea wave project (JONSWAP)," in *Suppl. A, Deutches Hydrographisches Institut, Hamburg*, 1973, pp. 433–438.
[46] M. Eriksson, J. Isberg, and M. Leijon, "Theory and experiment on an elastically moored cylindrical buoy," *IEEE J. Ocean. Eng.*, vol. 31, no. 4, pp. 959–963, Oct. 2006.
[47] R. Ahamed, K. McKee, and I. Howard, "A review of the linear generator type of wave energy Converters' power take-off systems," *Sustainability*, vol. 14, no. 16, p. 9936, Aug. 2022.
[48] F. Bizzozero, M. Giassi, G. Gruosso, S. Bozzi, and G. Passoni, "Dynamic model, parameter extraction, and analysis of two topologies of a tubular linear generator for seawave energy production," in *Proc. Int. Symp. Power Electron., Electr. Drives, Autom. Motion*, Jun. 2014, pp. 433–438.

[49] S. Bozzi, A. M. Miquel, F. Scarpa, A. Antonini, R. Archetti, G. Passoni, and G. Gruosso, "Wave energy production in Italian offshore: Preliminary design of a point absorber with tubular linear generator," in *Proc. Int. Conf. Clean Electr. Power (ICCEP)*, Jun. 2013, pp. 203–208.
[50] S. J. Chapman, *Electric Machinery Fundamentals*. New York, NY, USA: McGraw-Hill, 2004.
[51] I. Boldea and S. A. Nasar, "Linear electric actuators and generators," *IEEE Trans. Energy Convers.*, vol. 14, no. 3, pp. 712–717, Sep. 1999.
[52] A. El Magri, F. Giri, G. Besançon, A. El Fadili, L. Dugard, and F. Z. Chaoui, "Sensorless adaptive output feedback control of wind energy systems with PMS generators," *Control Eng. Pract.*, vol. 21, no. 4, pp. 530–543, Apr. 2013.
[53] W. Xiao, W. G. Dunford, P. R. Palmer, and A. Capel, "Application of centered differentiation and steepest descent to maximum power point tracking," *IEEE Trans. Ind. Electron.*, vol. 54, no. 5, pp. 2539–2549, Oct. 2007.
[54] R. M. Linus and P. Damodharan, "Maximum power point tracking method using a modified perturb and observe algorithm for grid connected wind energy conversion systems," *IET Renew. Power Gener.*, vol. 9, no. 6, pp. 682–689, Aug. 2015.
[55] L. Wang, S. Chai, D. Yoo, L. Gan, and K. Ng, *PID and Predictive Control of Electrical Drives and Power Converters Using MATLAB/Simulink*. Hoboken, NJ, USA: Wiley, 2015.

ABDIN Y. ELAMIN (Graduate Student Member, IEEE) received the B.Eng. degree (Hons.) in mechatronics engineering from International Islamic University Malaysia, in 2014, the M.Eng. degree in mechatronics and automatic control from the University of Technology Malaysia, in 2017, and the Ph.D. degree in electrical engineering from United Arab Emirates University, in 2023. In 2018, he was a Lecturer with the Control Department, University of Medical Science and Technology, Sudan. Currently, he is a Research Assistant with United Arab Emirates University. His research interests include model predictive control, artificial intelligence, and control applications in renewable energy and electromechanical systems.

ADDY WAHYUDIE (Member, IEEE) received the B.Eng. degree in electrical engineering from Gadjah Mada University, Indonesia, in 2002, the M.Eng. degree in electrical engineering from Chulalongkorn University, Thailand, in 2005, and the D.Eng. degree in electrical engineering from Kyushu University, Japan, in 2010. From 2005 to 2011, he was a Lecturer with the Department of Electrical Engineering, Gadjah Mada University. In 2011, he joined United Arab Emirates University as an Assistant Professor. He is currently an Associate Professor with the Department of Electrical Engineering, UAE University. His research interests include control systems applications in electromechanical and renewable energy systems (ocean wave energy).

TUANKU BADZLIN HASHFI received the B.Eng. degree (Hons.) in electrical and electronics engineering from the National University of Malaysia, Selangor, Malaysia, in 2015, and the M.Eng.Sc. degree from the University of Malaya, Malaysia, in 2021. He is currently pursuing the Ph.D. degree with TU Delft, The Netherlands. He was with United Emirates Arab University (UAEU) as a Research Assistant, until 2024. His research interests include DC/DC converters, AC/DC converters, multilevel converters, modular multilevel converters (MMC), the control strategies, renewable energy conversion, and high voltage direct current (HVDC).

HUSSAIN SHAREEF (Member, IEEE) received the B.Sc. degree (Hons.) in electrical and electronics engineering from the Institute of Information Technology, Dhaka, Bangladesh, in 1999, the M.Sc. degree in electrical and electronics engineering from Middle East Technical University, Ankara, Türkiye, in 2002, and the Ph.D. degree in electrical engineering from Universiti Teknologi Malaysia, Johor Bahru, Malaysia, in 2007. He is currently a Professor with the Department of Electrical Engineering, United Arab Emirates University, Al Ain, United Arab Emirates. His current research interests include power system optimization, power quality, artificial intelligence, renewable energy, and power system automation.

RACHID ERROUISSI (Senior Member, IEEE) received the Ph.D. degree in electrical engineering from the University of Quebec, Chicoutimi, QC, Canada, in 2010. From 2011 to 2014, he was a Postdoctoral Researcher with the ECE Department, University of New Brunswick. Since January 2019, he has been with the Department of Electrical Engineering, United Arab Emirates University (UAEU), as an Assistant Professor. His research interests include advanced controls, disturbance observer approach, electric machines and drives, and renewable energy conversion systems.

MOHAMMAD SHAKEEL LAGHARI received the B.E. degree in electronic engineering from the Mehran University of Engineering and Technology, Jamshoro, Pakistan, in 1980, the M.S. degree in electrical engineering from Drexel University, Philadelphia, PA, USA, in 1983, and the Ph.D. degree in computer engineering from the University of Wales, Swansea, Wales, U.K., in 1993. He was an Assistant Professor with Kuwait University and King Saud University. He is currently an Associate Professor with the Department of Electrical and Communication Engineering, United Arab Emirates University, Al Ain, United Arab Emirates. His research interests include applied artificial intelligence, image processing, and software systems. He has published more than 90 articles in these areas. He is a member of the IACSIT (Singapore), P.E.C. (Pakistan), UACEE (USA), and IRED (USA).

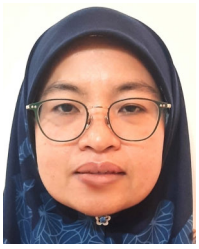

MARIZAN BINTI MUBIN received the B.Eng. degree in telecommunication engineering from the University of Malaya, Kuala Lumpur, in 2000, the M.Sc. degree in communications and signal processing from the University of Newcastle Upon Tyne, U.K., in 2001, and the D.Eng. degree in electrical engineering from Tokai University, Japan, in 2006. She is currently an Associate Professor with the Department of Electrical Engineering, University of Malaya.

SAAD MEKHILEF (Fellow, IEEE) received the B.Eng. degree in electrical engineering from the University of Sétif, Sétif, Algeria, in 1995, and the master's degree in engineering science and the Ph.D. degree in electrical engineering from the University of Malaya, Kuala Lumpur, Malaysia, in 1998 and 2003, respectively. He is currently a Professor and the Director of the Power Electronics and Renewable Energy Research Laboratory, Department of Electrical Engineering, University of Malaya. He is also the Dean of the Faculty of Engineering, University of Malaya. He is also a Distinguished Adjunct Professor with the School of Software and Electrical Engineering, Faculty of Science, Engineering and Technology, Swinburne University of Technology, VIC, Australia. He has authored more than 450 publications in international journals and conference proceedings. His current research interests include power converter topologies, control of power converters, renewable energy, and energy efficiency.